Article

Atmospheric Chemistry of *N*-Methylmethanimine (CH₃N═CH₂): A Theoretical and Experimental Study

Published as part of The Journal of Physical Chemistry virtual special issue "10 Years of the ACS PHYS Astrochemistry Subdivision".

Arne Joakim C. Bunkan,* Nina G. Reijrink, Tomáš Mikoviny, Markus Müller, Claus J. Nielsen,* Liang Zhu, and Armin Wisthaler

Read Online

ACCESS | 📊 Metrics & More | 📖 Article Recommendations | 🔵 Supporting Information

ABSTRACT: The OH-initiated photo-oxidation of *N*-methylmethanimine, CH₃N═CH₂, was investigated in the 200 m³ EUPHORE atmospheric simulation chamber and in a 240 L stainless steel photochemical reactor employing time-resolved online FTIR and high-resolution PTR-ToF-MS instrumentation and in theoretical calculations based on quantum chemistry results and master equation modeling of the pivotal reaction steps. The quantum chemistry calculations forecast the OH reaction to primarily proceed via H-abstraction from the ═CH₂ group and π-system C-addition, whereas H-abstraction from the −CH₃ group is a minor route and forecast that N-addition can be disregarded under atmospheric conditions. Theoretical studies of CH₃N═CH₂ photolysis and the CH₃N═CH₂ + O₃ reaction show that these removal processes are too slow to be important in the troposphere. A detailed mechanism for OH-initiated atmospheric degradation of CH₃N═CH₂ was obtained as part of the theoretical study. The photo-oxidation experiments, obstructed in part by the CH₃N═CH₂ monomer−trimer equilibrium, surface reactions, and particle formation, find CH₂═NCHO and CH₃N═CHOH/CH₂═NCH₂OH as the major primary products in a ratio 18:82 ± 3 (3σ-limit). Alignment of the theoretical results to the experimental product distribution results in a rate coefficient, showing a minor pressure dependency under tropospheric conditions and that can be parametrized $k(T)$ = 5.70 × 10⁻¹⁴ × $(T/298 \text{ K})^{3.18}$ × exp(1245 K/T) cm³ molecule⁻¹ s⁻¹ with k_{298} = 3.7 × 10⁻¹² cm³ molecule⁻¹ s⁻¹. The atmospheric fate of CH₃N═CH₂ is discussed, and it is concluded that, on a global scale, hydrolysis in the atmospheric aqueous phase to give CH₃NH₂ + CH₂O will constitute a dominant loss process. N₂O will not be formed in the atmospheric gas phase degradation, and there are no indications of nitrosamines and nitramines formed as primary products.
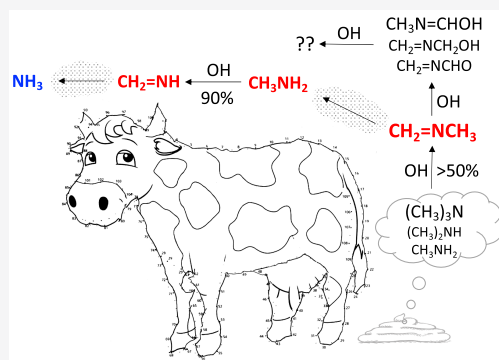
1. INTRODUCTION

Imines have been detected as major products in the atmospheric gas phase photo-oxidation of amines,[1−9] with *N*-methylmethanimine (CH₃N═CH₂, MMI) accounting for around 70% of the products formed in dimethylamine and 50% in trimethylamine photo-oxidation.[4] Amines are normally found in the low ppbv-range in the natural atmosphere, with methylamine, dimethylamine, and trimethylamine being among the most abundant.[10] Animal husbandry, oceans, and biomass burning are the major sources of methylamines, and cattle are estimated to account for 25% of all methylamine, 33% of all dimethylamine, and 55% of all trimethylamine emissions.[11] It has recently been established that methylamine and dimethylamine are also among the process degradation products of the more complex amines used in CO₂ capture,[12] and they may therefore always be present in the cleaned flue gas, no matter which parent amine that is used in the CO₂ capture process.

Experimental information on the atmospheric chemistry of imines is scarce; a possible and plausible explanation is that imines are prone to adsorb on surfaces, where they may hydrolyze (>C═NR + H₂O → >C═O + H₂NR),[13] and/or undergo a reversible trimerization reaction to form the corresponding 1,3,5-triazinane.[14] Tuazon and co-workers[15] detected MMI as product in the (CH₃)₂NH and (CH₃)₃N reactions with O₃ and reported the compound to be essentially nonreactive toward O₃ contrary to an earlier suggestion that the O₃ reaction with MMI leads to CH₃NO₂ and CH₂O.[16] Lazarou and Papagiannakopoulos studied the reaction of MMI
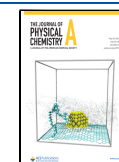
with Cl atoms employing the "very low pressure reactor" technique and reported $k_{CH_3N=CH_2+Cl} = (1.9 \pm 0.15) \times 10^{-11}$ cm^3 molecule^{-1} s^{-1} at 303 K,[17] which is comparable to the low pressure rate coefficient for the $CH_3CH=CH_2$ + Cl reaction (4×10^{-11} cm^3 molecule^{-1} s^{-1} at p = 0.44 mbar).[18] The early study of emission of aliphatic amines from animal husbandry by Schade and Crutzen[11] includes a speculative atmospheric degradation mechanism for MMI that potentially could lead to N_2O formation.

There are no previous reliable experimental literature data on products formed in atmospheric imine photo-oxidation; the first MMI photo-oxidation studies were carried out as part of the Norwegian "CO$_2$ and Amines Screening Study for Environmental Risks".[19] The experiments were hampered by aerosol formation and heterogeneous reactions to the extent that no conclusions were offered.[4] Recent results from theoretical studies of the OH radical reaction with the simplest imine, $CH_2=NH$, imply that this reaction primarily proceeds via H-abstraction with $k_{CH_2=NH+OH}$ in the range $(3-4) \times 10^{-12}$ cm^3 molecule^{-1} s^{-1} at 298 K[20,21] and that the major product under atmospheric conditions is HCN.[20]

The present communication reports results from a series of MMI photo-oxidation experiments in the EUPHORE atmospheric simulation chamber, the Oslo stainless steel photochemical reactor, and quantum chemistry based evaluations of the MMI + OH gas phase kinetics and major routes in the OH initiated photo-oxidation of MMI under atmospheric conditions.

2. METHODS

2.1. Experimental Methods and Chemicals. A series of experiments was carried out in chamber B in the EUPHORE facility at CEAM (Valencia, Spain, 39°28′12″N, 00°22′35″W); local time = UTC + 2 during the experiments. The facility and analytical methods have previously been reported in detail;[20] special online instrumentation employed in the present experiments include a high-resolution PTR-ToF 8000 instrument ($m/\Delta m > 3000$) from Ionicon Analytik GmbH, interfaced to the EUPHORE chamber via a Sulfinert-passivated stainless-steel tube (length, 125 cm; inner diameter, 5.33 mm; temperature, 75 °C; flow, 11 lpm). A flow of 0.16 lpm was branched off from this main inlet flow into a shortened, 10 cm PEEK inlet capillary. Subsequently, a sample flow of 0.025 lpm was branched off into the PTR-ToF-MS drift tube for analysis (inlet capillary and the drift tube both temperature-controlled at 75 °C). The drift tube was operated at an electric field strength E/N 88 Td (1 Td = 10^{-21} V m^2).

In a typical experiment, 1,3,5-trimethyl-1,3,5-triazinane (TMT) was evaporated and flushed into the chamber giving an initial mixing ratio in the range from 50 to 200 ppb. The canopy of the chamber was kept closed for several hours, during which time TMT slowly entered toward equilibrium with MMI, and NO/NO$_2$ and an OH-radical precursor were added. The photo-oxidation was followed for around 1 h, after which the chamber was closed and flushed overnight with scrubbed air.

Further MMI and TMT photo-oxidation experiments were carried out in the Oslo 240 L stainless steel Smog Chamber employing FTIR and high-resolution PTR-ToF-MS detection; the system was recently described in detail (in the present experiments the PTR drift tube was operated at 107 Td).[22] MMI was added to the evacuated chamber by heating a TMT

sample to 180 °C and trapping impurities and TMT in two dry ice cold-traps on the fly. TMT and an OH-radical precursor were added to the chamber by injection in a constant stream of replenishment air compensating for the PTR sampling.

Infrared absorption cross sections of TMT were obtained from calibrated spectra obtained of the pure gas at 294 ± 2 K in a cell of 9.85 ± 0.10 cm equipped with CsI windows. The spectra were recorded in the region 4000−400 cm^{-1} using a Bruker IFS 66v FTIR spectrometer equipped with a Ge/KBr beam splitter and employing a nominal resolution of 0.5 cm^{-1}. Single channel spectra were recorded averaging 128 interferograms applying Boxcar apodization. To ensure optical linearity, a DTGS detector was used. The pressure in the cells ranged from 1 to 10 mbar and was measured using CERAVAC CTR 100 transmitters with an accuracy of 0.2% of reading (Oerlicon Leybold Vacuum). The absorption spectrum of a 50 ppm·m TMT sample is shown in Figure S1 in the Supporting Information. Figure S2 shows two spectra of MMI/TMT obtained at 80 min intervals and a synthetic spectrum of MMI obtained by spectral subtraction is presented in Figure S3; the figure also includes the vibrational assignment of MMI.[23,24] It should be noted that the absorption cross sections of MMI are almost an order of magnitude smaller than those of TMT.

1,3,5-Trimethyl-1,3,5-triazinane (Sigma-Aldrich, 97%) and 2-propanol 3,3,3,6,6,6-d_6 (Sigma-Aldrich, 99 atom % D) were used without further purification. N-Methylmethanimine was prepared by heating 1,3,5-trimethyl-1,3,5-triazinane to 180 °C and trapping the vapor at liquid nitrogen temperature. 2-Propyl nitrite (isopropyl nitrite, IPN) and 2-propyl nitrite 3,3,3,6,6,6-d_6 (IPN-d_6) were synthesized from sulfuric acid, sodium nitrite, and 2-propanol or 2-propanol-3,3,3,6,6,6-d_6 and purified by repeated washing with ice water.

2.2. Computational Methods. Geometry optimization of stationary points on the potential energy surface (PES) of the OH reaction with $CH_3N=CH_2$ was made in MP2[25] and M06-2X density functional[26] calculations employing Dunning's correlation-consistent aug-cc-pVTZ basis sets.[27,28] The subsequent atmospheric reactions were characterized in M06-2X calculations. Energies of stationary points on the reaction surfaces were improved by explicitly correlated CCSD(T) calculations with scaled triples contributions, CCSD(T*)-F12a,[29] in the following abbreviated CC. Excited states and surface crossings were explored in TD-DFT, CIS, and CASSCF calculations. Additional dipole moments and isotropic polarizabilities, serving as input to prediction of ion−molecule reaction rate coefficients,[30] were obtained in B3LYP calculations; the results are summarized in Table S1 in the Supporting Information. Reaction enthalpies were calculated using the G4 multilevel method.[31] The M06-2X (tight optimization criteria and ultrafine integration grids), B3LYP, CIS, CASSCF, MP2, and G4 calculations were performed with Gaussian09[32] and Gaussian16,[33] whereas the coupled cluster calculations were carried out with Molpro 2019.2.[34]

Master equation calculations were carried out using the Master Equation Solver for Multi-Energy-well Reactions (MESMER v.4.1)[35] to simulate the kinetics of the OH radical reactions with CH_3NCH_2 and the branching in consecutive reactions under atmospheric conditions. The required input parameters for molecules, intermediate species and products were obtained from the ab initio calculations. Tunneling corrections were approximated in the models employing a one-dimensional asymmetrical Eckart barrier using the method
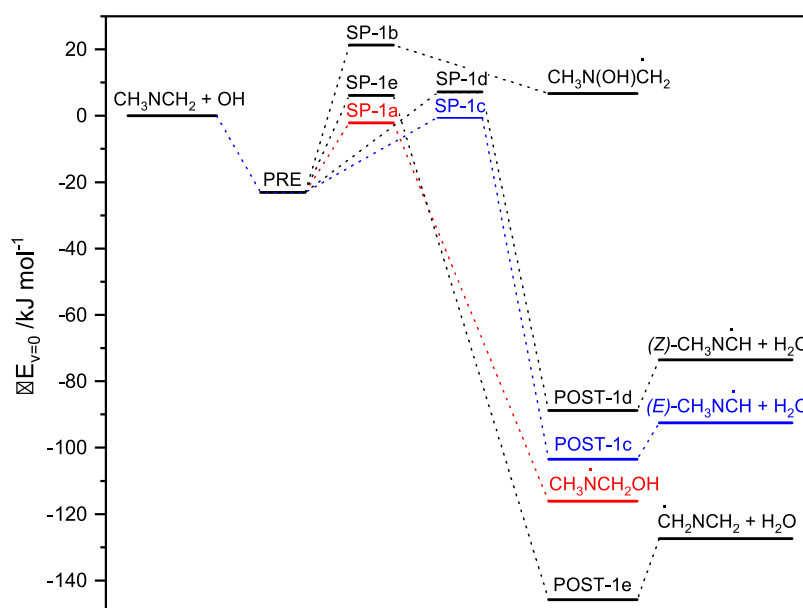
Figure 1. Relative energies of stationary points on the potential energy surface of the CH$_3$N=CH$_2$ + OH reaction. Results from CCSD(T*)-F12a/aug-cc-pVTZ//M06-2X/aug-cc-pVTZ calculations.

described by Miller.[36] Rate coefficients for barrierless association reactions were approximated by $k_{association}$ = 4.0 × 10^{-10} × $(T/298$ K$)^{1/6}$ from long-range transition state theory.[37] Spin−orbit coupling in the OH radical (139.7 cm^{-1})[38] was included in the model by lowering the energy of the OH radical with half of the splitting and including the ^{2}P$_{3/2}$ and ^{2}P$_{1/2}$ spin−orbit states in the electronic partition function. It was assumed that spin−orbit coupling could be neglected in the prereaction adduct and in the saddle points.

Lennard-Jones parameters for the CH$_3$N=CH$_2$ + OH reactions were approximated by values for methyl acetate (ε = 469.8 K, σ = 4.94 Å)[39] having a similar number of atoms and dipole moment as the prereaction adduct, and the energy transfer in collisions with N$_2$ and O$_2$, $\langle \Delta E_{down} \rangle$, was set to 250 cm^{-1}. Variation of these parameters resulted in only insignificant changes in the calculated rate coefficients; changing $\langle \Delta E_{down} \rangle$ by ±50 cm^{-1} resulted in changes of ±0.5% in the overall rate coefficients; changing the Lennard-Jones parameters by ±50% resulted in changes of <1.5% in the overall rate coefficients.

3. RESULTS AND DISCUSSION

3.1. Computational Results. The initial step in the CH$_3$N=CH$_2$ reaction with OH radicals will either be an addition to the π-system or a hydrogen abstraction; the reaction enthalpies listed stem from G4 calculations and refer to 1013 mbar and 298 K:

$$CH_3N{=}CH_2 + OH \rightarrow CH_3N^{\bullet}{-}CH_2OH$$

$$\Delta H^{\ominus} = -119 \text{ kJ mol}^{-1} \qquad (1a)$$

$$\rightarrow CH_3N(OH){-}C^{\bullet}H_2 \quad \Delta H^{\ominus} = +1 \text{ kJ mol}^{-1} \qquad (1b)$$

$$\rightarrow (E)\text{-}CH_3N{=}C^{\bullet}H + H_2O \quad \Delta H^{\ominus} = -90 \text{ kJ mol}^{-1} \qquad (1c)$$

$$\rightarrow (Z)\text{-}CH_3N{=}C^{\bullet}H + H_2O \quad \Delta H^{\ominus} = -71 \text{ kJ mol}^{-1} \qquad (1d)$$

$$\rightarrow C^{\bullet}H_2N{=}CH_2 + H_2O \quad \Delta H^{\ominus} = -124 \text{ kJ mol}^{-1} \qquad (1e)$$
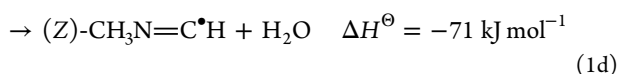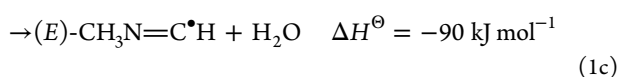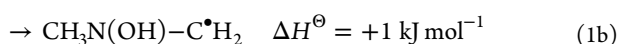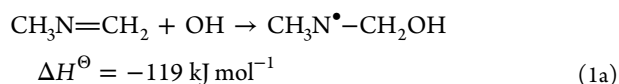
Figure 1 illustrates the relative energies of stationary points on the potential energy surface (PES) of the initial CH$_3$NCH$_2$ + OH reaction; the underlying quantum chemistry data are summarized in Table S2 (energies, T_1[40] and D_1[41,42] diagnostics values, vibrational frequencies, rotational constants, and Cartesian coordinates of the stationary points). The T_1 diagnostic values for the saddle points are all significantly below 0.044 (the largest value being 0.036 for the SP-1c), indicating that the coupled cluster calculations are not seriously affected by multireference problems.[40,42]

All routes, with the exception of (1b), are calculated to be exothermic proceeding via a common prereaction adduct (PRE), and to have barriers below 10 kJ mol^{-1}. The CC//M06-2X results point to reactions 1a and 1c as the more important pathways having submerged saddle points at −2.1 and −0.5 kJ mol^{-1}, respectively, whereas reactions 1d and 1e with barriers of 7.0 and 6.1 kJ mol^{-1} will constitute minor pathways. The N-addition route, having a calculated barrier of 21.3 kJ mol^{-1}, is of no importance under atmospheric conditions.

The CC//MP2 calculations (Table S2) give somewhat higher barriers of 3.3, 32.2, 0.9, 12.5, and 18.4 kJ mol^{-1}, respectively. The MP2 saddle point structures are distinctively closer to the product sides of reaction than the M06-2X structures, and they also show significantly steeper potentials, Table S2. The difference between the CC//MP2 and CC//M06-2X results can conveniently be divided into contributions from the coupled cluster electronic energy (Δ_{CC}) and the zero-point energy (Δ_{ZPE}) that is negligible for the reactants (Δ_{CC} = −0.1, Δ_{ZPE} = 0.1 kJ mol^{-1}), but substantial for PRE and the saddle points SP-1a through SP-1e: Δ_{CC}/Δ_{ZPE} = −3.0/17.4, 1.9/3.4, 7.5/3.4, −1.9/3.3, 1.8/3.8, and 5.2/7.2 kJ mol^{-1}, respectively. The unusual differences in calculated ZPEs are related to an inappropriate MP2 description of the π-system during the reaction that, in its most extreme, is manifested by bizarre vibrational wavenumbers such as $\tilde{v}_{C=N}$ = 4071 cm^{-1} in PRE and 2724 cm^{-1} in SP-1e, Table S2. The fact that the Δ_{CC}

values are relatively small, in spite of some structure differences being >0.1 Å, support the M06-2X description of the MMI + OH PES having wider potentials, over that of MP2.

3.1.1. Kinetics and Branching in the CH$_3$NCH$_2$ + OH Reaction. The kinetics of the CH$_3$NCH$_2$ + OH reaction may in principle be governed by both formation of the prereaction adduct and by one or more tight inner transition states. Microcanonical rate coefficients for the inner transition states were calculated using RRKM theory based on energies and rovibrational data from CC//M06-2X calculations. Rate coefficients for the outer transition state were calculated using the inverse Laplace transform of capture rate expressions of the form $k(T) = C \times (T/298 \text{ K})^{-1/6}$ from long-range transition state theory (LRTST)[37] assuming a dipole−dipole potential ($C = 4.0 \times 10^{-10}$ cm^3 molecule^{-1} s^{-1}, and calculated dipole moments are collected in Table S1). Long-range transition state theory results represent upper limits to the actual capture rates. Akbar and Barker[21] studied the influence of the prereaction complex on the reaction of methanimine and OH radicals with canonical variational transition state theory (CVTST) and reported that LRTST overestimated the formation rate by a factor of 2 in this system. The sensitivity of the calculated rate coefficient to variations in the capture rate was tested by varying C between 10^{-9} and 10^{-10} cm^3 molecule^{-1} s^{-1}; only minor changes in the overall and individual rates were found. It can be concluded that the reaction rate is controlled by the inner, tight transition states and that simple capture rate expressions like LRTST or even assuming the gas kinetic collision rate is sufficient for kinetic modeling of the present reaction.

The addition reactions, (1a) and (1b), were treated as reversible isomerization reactions, while the hydrogen abstraction routes (1c)−(1e) were treated as irreversible reactions. The transition states SP-1a, SP-1d, and SP-1e give rise to doubly degenerate reaction paths. The structure of SP-1c also seem to give a degenerate reaction path, but the two saddle points are connected by a rotation of the OH fragment with a small barrier only 0.7 kJ mol^{-1} above the entrance energy of the reactants, and are therefore treated as a single reaction path.

Rotation of the methyl group in MMI is hindered by a barrier calculated to be around 8.9 kJ mol^{-1} (~740 cm^{-1}), which is ~50 cm^{-1} higher than the experimental value for the CH$_3$ rotational barrier in propene.[43−45] The barrier is slightly higher in the prereaction complex (9.5 kJ mol^{-1}) and lowered in the saddle points SP-1a, SP-1c, and SP-1d to 5.8, 7.3, and 7.6 kJ mol^{-1}, respectively. On the exit side the CH$_3$ rotational barriers are further lowered to 4.0, 2.8, and 5.0 kJ mol^{-1}. The barriers to rotation of the OH fragment at the saddle points of reaction are very different in both shape and height; M06-2X calculations reveal barriers ranging from 3 to 25 kJ mol^{-1} (Figure S4).

The calculations imply that the hydrogen abstraction route (1c) leading to (E)-CH$_3$N═C$^{\bullet}$H is dominant at all temperatures and pressures relevant to the atmosphere. In the harmonic oscillator approximation, the branching between reactions 1a−1e is calculated to be 41:0:53:2:4 with a total rate coefficient of 1.4×10^{-12} cm^3 molecule^{-1} s^{-1} at SATP (298 K, 1000 mbar). Including tunneling in the model increases k_{SATP} to 1.9×10^{-12} cm^3 molecule^{-1} s^{-1} and modifies the branching to 39:0:50:3:8. Treating the CH$_3$ and OH torsional motions as hindered internal rotors in the master equation calculations and employing the above-mentioned calculated rotational

potentials changes k_{SATP} to 3.3×10^{-12} cm^3 molecule^{-1} s^{-1} and the branching to 27:0:64:3:6.

Ab initio calculated vibrational frequencies are often multiplied by a scale factor to compensate in part for the electronic structure calculation being approximate and for the potential energy surface not being harmonic. For M06-2X/aug-cc-pVTZ calculations, the recommended scaling factor is 0.958,[46] and employing this scaling to the vibrational frequencies in the model increases k_{SATP} to 3.5×10^{-12} cm^3 molecule^{-1} s^{-1} and alters the branching to 25:0:64:4:7.

The rate coefficient at SATP is comparable to that of the CH$_2$═NH + OH reaction, calculated in a similar way (3.0^{20} and $4.0^{21} \times 10^{-12}$ cm^3 molecule^{-1} s^{-1}), and is almost an order of magnitude smaller than the recommended high-pressure value for the CH$_3$CH═CH$_2$ reaction with OH.[47] In this context it should be noted that the CH$_3$CH═CH$_2$ + OH reaction is entirely an addition reaction under atmospheric conditions, whereas the CH$_3$N═CH$_2$ + OH reaction—like the CH$_2$═NH + OH reaction[20,21]—proceeds via both addition and H−abstraction.

Considering an uncertainty of ± 4 kJ mol^{-1} in the calculated saddle point heights, we arrive at the following unpretentious limits for the branching ratios, Γ_i, at 298 K: 7% < Γ_{1a} < 56%, Γ_{1b} < 0.01%, 34% < Γ_{1c} < 90%, Γ_{1d} < 13%, Γ_{1e} < 12%, and an uncertainty factor of 5 for the total rate coefficient (model sensitivity matrix presented in Table S3).

3.1.2. Atmospheric Photo-oxidation. On a global scale, reaction with OH radicals is the dominant gas phase loss process for a majority of tropospheric trace gases.[48] Other relevant atmospheric oxidants include ozone, Cl atoms, and NO$_3$ radicals; the rate coefficient for the Cl atom reaction with MMI has been reported,[17] and the rate coefficient for NO$_3$ radical reaction with MMI can to a first approximation be estimated from the "linear free energy relationship" between OH and NO$_3$ radical reactions.[49]

The present theoretical study addresses the OH-initiated photo-oxidation of MMI, the MMI + O$_3$ reaction, and the tropospheric photolysis of MMI. Only primary products are considered, and for the sake of simplicity, we have not attended minor routes in the atmospheric photo-oxidation (RO$_2$ + RO$_2$ → R$_{-H}$O + ROH + O$_2$, RO$_2$ + RO$_2$ → RO + RO + O$_2$, RO$_2$ + HO$_2$ → ROOH + O$_2$, RO$_2$ + NO$_3$ → RO + NO$_2$ + O$_2$, and RO$_2$ + NO → RONO$_2$).

3.1.2.1. Fate of the CH$_3$N$^{\bullet}$CH$_2$OH Radical. The kinetic calculations indicate that ~30% of the initial CH$_3$N═CH$_2$ + OH reaction will follow the C-addition route:

$$CH_3N\text{═}CH_2 + OH \rightarrow CH_3N^{\bullet}\text{−}CH_2OH^{\ddagger}$$
$$\Delta H^{\ominus} = -119 \text{ kJ mol}^{-1} \tag{1a}$$
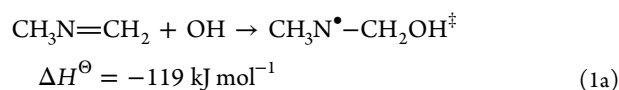
The reaction is highly exothermic, and the activated CH$_3$N$^{\bullet}$CH$_2$OH‡ radical may conceivably isomerize with a rate potentially orders of magnitude faster than any competing bimolecular reactions:

$$CH_3N^{\bullet}CH_2OH^{\ddagger} \rightleftarrows CH_3NHCH_2O^{\bullet\ddagger}$$
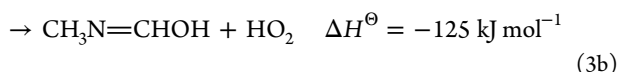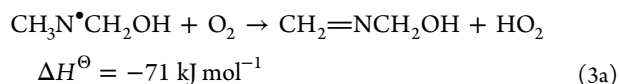$$\Delta H^{\ominus} = +37 \text{ kJ mol}^{-1} \tag{2}$$
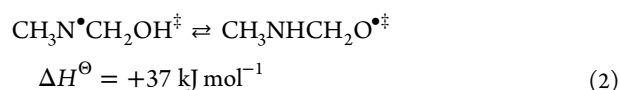
The unimolecular isomerization reaction 2 is, however, calculated with a high barrier of around 120 kJ mol^{-1}, which roughly places it at the energy of the initial reactants in reaction 1a. Table S4 summarizes the relative energies of stationary points on the CH$_3$N$^{\bullet}$CH$_2$OH radical formation and
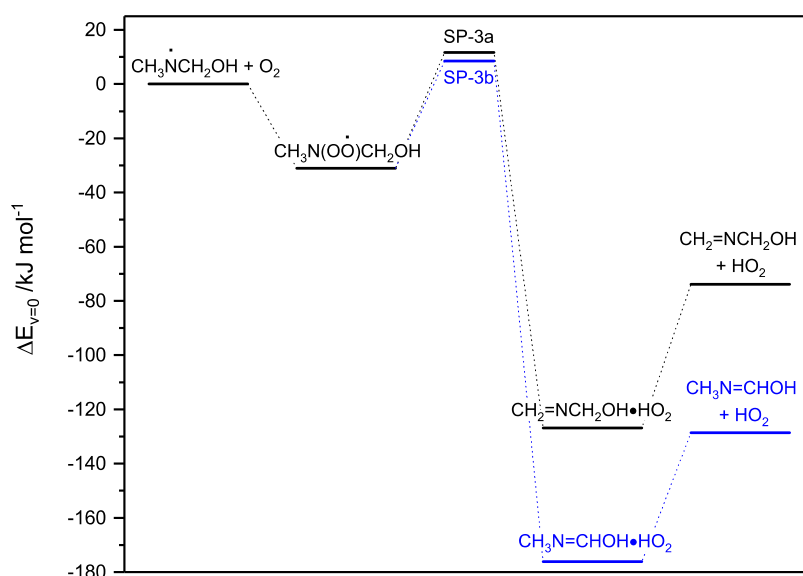
Figure 2. Relative energies of stationary points on the potential energy surface of the $CH_3N^\bullet CH_2OH + O_2$ reaction and the subsequent isomerization/dissociation reactions. Results from CCSD(T*)-F12a/aug-cc-pVTZ//M06-2X/aug-cc-pVTZ calculations.

subsequent isomerization reaction including the relevant underlying quantum chemistry data. The rate coefficient for isomerization of thermalized $CH_3N^\bullet CH_2OH$ radicals is calculated to be $k_2 \approx 1.6 \times 10^{-6}$ s^{-1} under atmospheric conditions, and a master equation model of reaction 2 shows that less than 0.1% of the activated $CH_3N^\bullet CH_2OH^\ddagger$ radicals will actually undergo isomerization before being thermalized. It can therefore be concluded that the isomerization reaction 2 will not be significant under atmospheric conditions.
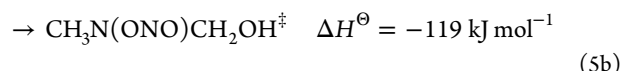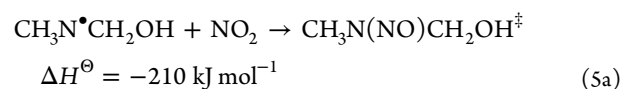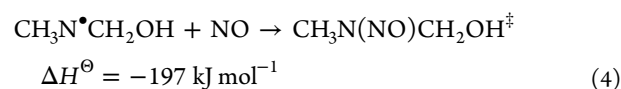
Following results from experimental studies of the $CH_3N^\bullet CH_3$ radical reactions,[1,2,4,50] the $CH_3N^\bullet CH_2OH$ radical may conceivably react with O_2, NO, and NO_2. There are two routes in the O_2 reaction, both proceeding via the $>NOO^\bullet$ radical on the entrance side, medium sized barriers of respectively 11.7 and 8.5 kJ mol^{-1}, and HO_2 post reaction complexes on the exit side as illustrated in Figure 2 (the underlying quantum chemistry data are summarized in Table S5). For comparison, the barrier to the corresponding $CH_3N^\bullet CH_3 + O_2$ reaction is calculated to be 21.5 kJ mol^{-1} at the same level of theory.

$$CH_3N^\bullet CH_2OH + O_2 \rightarrow CH_2{=}NCH_2OH + HO_2$$
$$\Delta H^\ominus = -71 \text{ kJ mol}^{-1} \tag{3a}$$

$$\rightarrow CH_3N{=}CHOH + HO_2 \quad \Delta H^\ominus = -125 \text{ kJ mol}^{-1} \tag{3b}$$

Reaction 3 was investigated in a master equation model based on the PES illustrated in Figure 2. The $CH_3N^\bullet CH_2OH$ + O_2 association reaction was treated as reversible with $k_{association} = 10^{-10}$ cm^3 molecule^{-1} s^{-1} and the post reaction complexes, $CH_2{=}NCH_2OH\bullet HO_2$ and $CH_3N{=}CHOH\bullet$-HO_2, were assumed to dissociate instantaneously to the reaction products; treating dissociation of the postreaction complexes explicitly makes no difference to the outcome of the kinetic modeling. The CNOO torsional mode in CH_3N-$(OO^\bullet CH_2OH$ was described as a hindered internal rotor (the potential obtained in M06-2X calculations is shown in Figure S5).

The model predicts $k_3 = 1.4 \times 10^{-14}$ cm^3 molecule^{-1} s^{-1} at 298 K and a branching (3a):(3b) $\approx$ 1:99 when tunneling is included. The model is not very sensitive to the association rate; reducing $k_{association}$ by an order of magnitude lowers the calculated rate coefficient by less than 5%. The model predicts $k_3 = 1.2 \times 10^{-16}$ cm^3 molecule^{-1} s^{-1} at 298 K and a branching (3a):(3b) $\approx$ 10:90 when tunneling is not integrated; the changed branching ratio is due to quite different imaginary vibrational wavenumbers at the saddle points, Table S5. Uncertainties in the barrier heights were considered by reducing SP-3a by 4 and increasing SP-3b by 4 kJ mol^{-1} at the same time; this extreme results in a branching of 73:27 when tunneling is not integrated in the model.

The $CH_3N^\bullet CH_2OH$ radical reactions with NO and NO_2 both proceed without electronic barriers:

$$CH_3N^\bullet CH_2OH + NO \rightarrow CH_3N(NO)CH_2OH^\ddagger$$
$$\Delta H^\ominus = -197 \text{ kJ mol}^{-1} \tag{4}$$

$$CH_3N^\bullet CH_2OH + NO_2 \rightarrow CH_3N(NO)CH_2OH^\ddagger$$
$$\Delta H^\ominus = -210 \text{ kJ mol}^{-1} \tag{5a}$$

$$\rightarrow CH_3N(ONO)CH_2OH^\ddagger \quad \Delta H^\ominus = -119 \text{ kJ mol}^{-1} \tag{5b}$$

The activated $CH_3N(ONO)CH_2OH^\ddagger$ is metastable and will dissociate directly without any electronic barrier in addition to the reaction endothermicity:

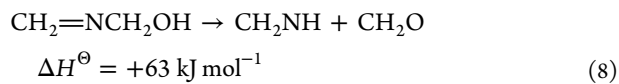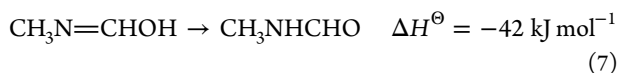$$CH_3N(ONO)CH_2OH^\ddagger \rightarrow CH_3N(O^\bullet)CH_2OH + NO$$
$$\Delta H^\ominus = +37 \text{ kJ mol}^{-1} \tag{6}$$
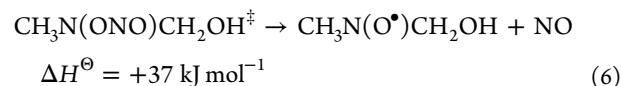
Although the $CH_3N^\bullet CH_2OH + NO/NO_2$ reactions may be very fast, the loss rate of $CH_3N^\bullet CH_2OH$ radicals due to reaction with O_2 will be in the range 6×10^2 to 7×10^4 s^{-1} under atmospheric conditions, which in any case will be orders of magnitude faster than the competing reactions with realistic atmospheric ppb-levels of NO and NO_2. It can be concluded from the theoretical results that that the $CH_3N^\bullet CH_2OH$ radical reaction with O_2 is so fast that the competing (and
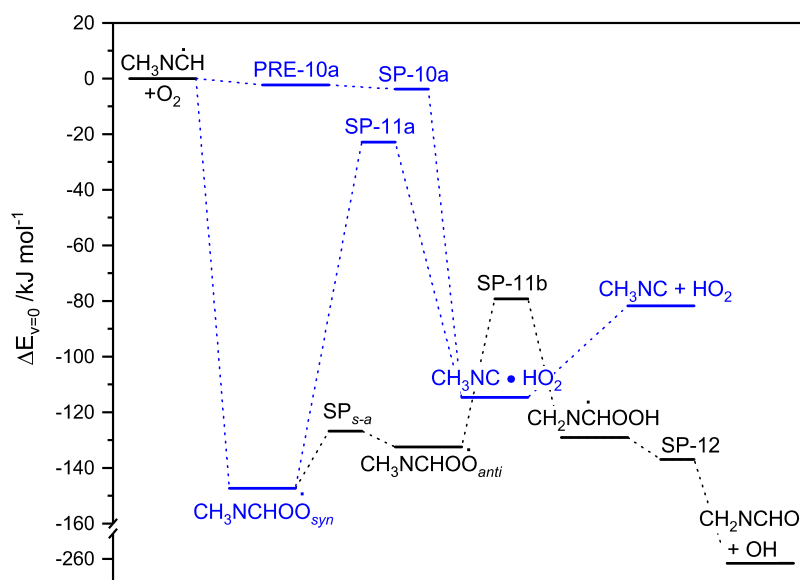
Figure 3. Relative energies of stationary points on the potential energy surface of the E-CH$_3$NC$^\bullet$H + O$_2$ reaction. Results from CCSD(T*)-F12a/aug-cc-pVTZ//M06-2X/aug-cc-pVTZ calculations.

barrierless) reactions with NO and NO$_2$ are of little importance under atmospheric conditions. That is, insignificant nitrosamine and/or nitramine formation will result in the atmospheric reactions of the CH$_3$N$^\bullet$CH$_2$OH radical. Concerning the branching in reaction 3, the present theoretical calculations cannot predict this accurately.

The two products formed in reaction 3 may in principle both undergo tautomerization reactions. N-methylformimidic acid (CH$_3$N=CHOH) can tautomerize to the E-conformation of N-methylformamide via a barrier of around 135 kJ mol^{-1} whereas the 1,3-H transfer in N-methanol methaneimine (CH$_2$=NCH$_2$OH), proceeding via a barrier near 185 kJ mol^{-1}, is calculated to dissociate spontaneously to methanimine and formaldehyde:

$$CH_3N=CHOH \rightarrow CH_3NHCHO \quad \Delta H^\Theta = -42 \text{ kJ mol}^{-1}$$
(7)

$$CH_2=NCH_2OH \rightarrow CH_2NH + CH_2O$$
$$\Delta H^\Theta = +63 \text{ kJ mol}^{-1}$$
(8)

Reaction 8 is clearly not relevant under atmospheric conditions, and a master equation model simulation of reaction 7 indicates $k_7 \times 5 \times 10^{-7}$ s^{-1} for thermalized CH$_3$N=CHOH at 1 atm and 298 K (thermal lifetime $\sim$20 d). The CH$_3$N=CHOH tautomerization to CH$_3$NHCHO (N-methyl formamide) is calculated with a barrier that is slightly higher than found for the corresponding HN=CHOH $\rightarrow$ H$_2$NCHO isomerization[20] (138.1 vs 119.7 kJ mol^{-1}, which results from M06-2X/aug-cc-pVTZ calculations), and will not be significant under atmospheric conditions—even should all the available enthalpy of reaction 3b be deposited in CH$_3$N=CHOH.

In summary, the theoretical calculations locate CH$_2$=NCH$_2$OH and CH$_2$N=CHOH as the dominating products resulting from the OH addition reaction 1a with <10% of the former and >90% of the latter. However, extreme conservative limits to the yields are <75% and >25%.
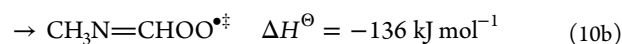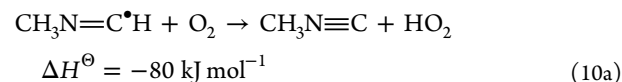
3.1.2.2. Fate of the CH$_3$NC$^\bullet$H radical. Around 70% of reaction 1 is predicted to give CH$_3$N=C$^\bullet$H radicals that are

formed predominantly as the low energy E-isomer; see Figure 1. There is a barrier of around 35 kJ mol^{-1} between the Z-isomer having around 19 kJ mol^{-1} higher energy than the $E-$isomer, and the unimolecular $Z \rightarrow E$ conversion rate at thermal equilibrium is estimated to be around 4×10^5 s^{-1}. Since the subsequent reactions of the Z- and E-isomers are the same, we only consider the low energy E-isomer in the following.

Direct H-ejection from the CH$_3$N=C$^\bullet$H radical is highly endothermic and can therefore be neglected under atmospheric conditions:

$$CH_3N=C^\bullet H \rightarrow CH_3NC + H \quad \Delta H^\Theta = +126 \text{ kJ mol}^{-1}$$
(9)
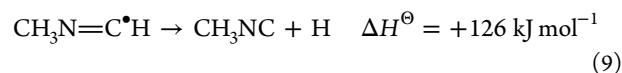
The main atmospheric sink for CH$_3$N=C$^\bullet$H is therefore reaction with O$_2$. Two routes have been identified: direct H-abstraction, resulting in CH$_3$NC, and the formation of an activated peroxy radical:

$$CH_3N=C^\bullet H + O_2 \rightarrow CH_3N\equiv C + HO_2$$
$$\Delta H^\Theta = -80 \text{ kJ mol}^{-1}$$
(10a)

$$\rightarrow CH_3N=CHOO^{\bullet\ddagger} \quad \Delta H^\Theta = -136 \text{ kJ mol}^{-1}$$
(10b)
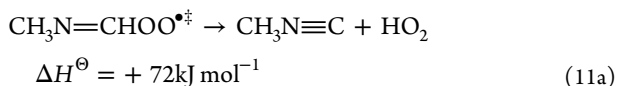
The H-abstraction reaction proceeds via a submerged barrier (SP-10a, $\Delta E_{elec} = -3$ kJ mol^{-1}) linked to a weak prereaction adduct on the entrance side (PRE-10a, $\Delta E_{elec} = -6$ kJ mol^{-1}, basis set superposition error $\approx$0.8 kJ mol^{-1}) and to a H-bonded HO$_2$ radical complex on the exit side. The vibrational zero-point energy of the prereaction adduct PRE-10a is around 5 kJ mol^{-1} larger than that of the saddle point SP-10a, apparently placing $\Delta E_{v=0}$(PRE-10a) > $\Delta E_{v=0}$(SP-10a). However, the T_1 diagnostic value for PRE-10a is 0.059, suggesting that the results of the coupled cluster calculations should be considered with caution.

There are two conformations of the CH$_3$N=CHOO$^\bullet$ radical separated by a few kJ mol^{-1} barrier—the low energy form has a synperiplanar HCOO moiety (syn); the high energy form ($\sim$+16 kJ mol^{-1}) has an antiperiplanar HCOO moiety ($anti$). The activated peroxy radical may initiate internal H-
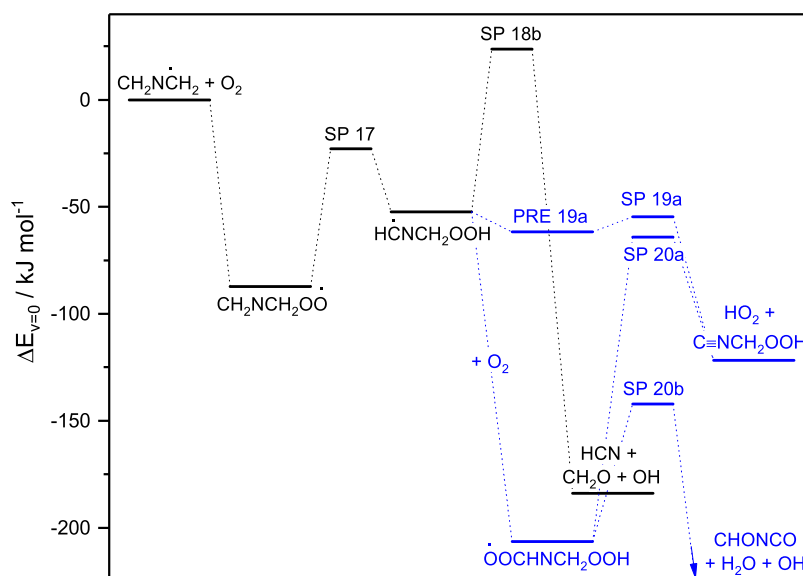
**Figure 4.** Relative energies of stationary points on the potential energy surface of the $CH_2=NC^\bullet H_2 + O_2$ reaction. Stationary points in black include the energy of an additional O_2. Results from CCSD(T*)-F12a/aug-cc-pVTZ//M06-2X/aug-cc-pVTZ calculations.

shift reactions with barriers below the entrance energy in reaction 10:

$$CH_3N=CHOO^{\bullet\ddagger} \rightarrow CH_3N\equiv C + HO_2$$
$$\Delta H^\Theta = +72 \, kJ \, mol^{-1} \tag{11a}$$

$$\rightarrow C^\bullet H_2N=CHOOH^\ddagger \quad \Delta H^\Theta = +23 \, kJ \, mol^{-1} \tag{11b}$$

The M06-2X calculations find the $C^\bullet H_2N=CHOOH$ radical to be metastable with an electronic barrier of only 7.5 kJ mol^{-1} to dissociation:

$$C^\bullet H_2N=CHOOH^\ddagger \rightarrow CH_2=NCHO + OH$$
$$\Delta H^\Theta = -129 \, kJ \, mol^{-1} \tag{12}$$
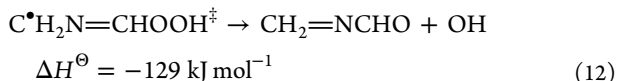
The couple cluster calculations, however, reverse the energies to -2.3 kJ mol^{-1}. Since the T_1-values are below 0.025 for both structures, we suggest that the alleged electronic barrier is an artifact of the M06-2X functional.

The $CH_3N=CHOO^\bullet$ peroxy radical may also react with NO to form the corresponding oxy radical that may either eject an H atom directly resulting in methyl isocyanate or undergo H-abstraction by O_2 to give the same product. H-ejection is endothermic and proceeds essentially without any additional electronic barrier.
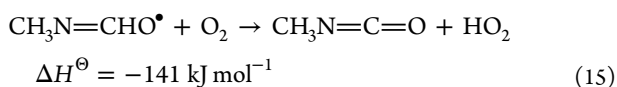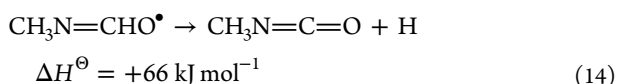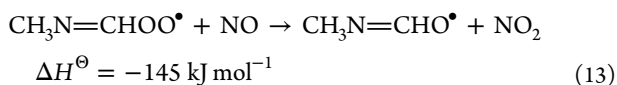
$$CH_3N=CHOO^\bullet + NO \rightarrow CH_3N=CHO^\bullet + NO_2$$
$$\Delta H^\Theta = -145 \, kJ \, mol^{-1} \tag{13}$$

$$CH_3N=CHO^\bullet \rightarrow CH_3N=C=O + H$$
$$\Delta H^\Theta = +66 \, kJ \, mol^{-1} \tag{14}$$

$$CH_3N=CHO^\bullet + O_2 \rightarrow CH_3N=C=O + HO_2$$
$$\Delta H^\Theta = -141 \, kJ \, mol^{-1} \tag{15}$$

Figure 3 shows the relative energies of stationary points on the $CH_3N=C^\bullet H + O_2$ PES; the underlying data are documented in Table S6. The $CH_3N=C^\bullet H + O_2$ reaction sequence, (10)–(12), was modeled in master equation calculations based on
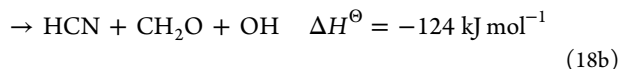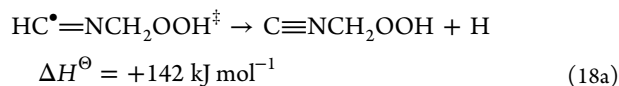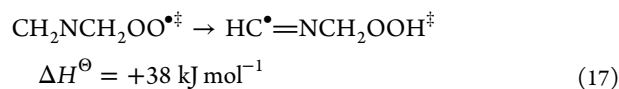
the PES illustrated in Figure 3, and including the sequence (13)–(15) as a competing RO_2-sink. The calculations reveal that direct H-abstraction (10a) is 2 orders of magnitude slower than the RO_2-routes initiated via (10b)—even when lowering the energy of PRE-10a by 20 kJ mol^{-1}—and that route (11b) dominates the atmospheric fate of the $CH_3N=CHOO^\bullet$ radical with a yield of >98%.

In conclusion, under atmospheric conditions N-methylene-formamide, $CH_2=NCHO$, will be the by far dominant product following H-abstraction from the CH_2-group in MMI.

3.1.2.3. Fate of the $CH_2NC^\bullet H_2$ radical. Less than 5% of the initial $CH_3N=CH_2 + OH$ reaction is predicted to result in $CH_2NC^\bullet H_2$ radicals that, under atmospheric conditions, will react with O_2 forming an activated peroxy radical:

$$CH_2NC^\bullet H_2 + O_2 \rightarrow CH_2NCH_2OO^{\bullet\ddagger}$$
$$\Delta H^\Theta = -94 \, kJ \, mol^{-1} \tag{16}$$
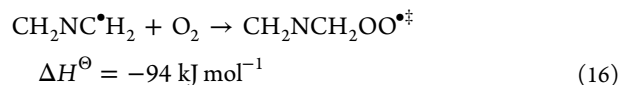
The addition reaction appears without any electronic barrier, and the activated peroxy-radical may undergo unimolecular reactions before being thermalized by collisions or entering bimolecular reactions. Potentially, a 1,5-H transfer may be followed by either H-ejection or dissociation:

$$CH_2NCH_2OO^{\bullet\ddagger} \rightarrow HC^\bullet=NCH_2OOH^\ddagger$$
$$\Delta H^\Theta = +38 \, kJ \, mol^{-1} \tag{17}$$

$$HC^\bullet=NCH_2OOH^\ddagger \rightarrow C\equiv NCH_2OOH + H$$
$$\Delta H^\Theta = +142 \, kJ \, mol^{-1} \tag{18a}$$

$$\rightarrow HCN + CH_2O + OH \quad \Delta H^\Theta = -124 \, kJ \, mol^{-1} \tag{18b}$$

The endothermic 1,5−H transfer reaction 17 has a barrier well below the entrance energy of the initial reactants, but the subsequent unimolecular reactions of $HC^\bullet=NCH_2OOH$ are hindered by barriers above the entrance energy. There is also a relatively high barrier of around 140 kJ mol^{-1} to direct H-ejection, and this route will therefore not be relevant under atmospheric conditions. Finally, the dissociation reaction 18b

is not a simple unimolecular dissociation; the quantum chemistry calculations show an initial barrier of around 20 kJ mol^{-1} above the entrance energy to give HCN and the metastable C$^{\bullet}$H$_2$OOH radical, which then dissociates to CH$_2$O and OH. The latter fine details have not been included in Figure 4 illustrating the relative energies of the stationary points on the PES of the CH$_2$NC$^{\bullet}$H$_2$ + O$_2$ reaction (energies and Cartesian coordinates of the stationary points of the reaction are summarized in Table S7).

As a consequence of the significant barriers to reaction 18, the atmospheric fate of CH$_2$NCH$_2$OO$^{\bullet}$ radicals will be determined by the competition between collisional quenching, reaction with NO, and the O$_2$ reaction with HC$^{\bullet}$=NCH$_2$OOH radicals. The latter autoxidation may either proceed via a direct or an indirect H-abstraction leading to C≡NCH$_2$OOH, or via an activated O$^{\bullet}$OCH=NCH$_2$OOH‡ peroxy-radical and a second internal 1,5−H transfer resulting in HOOCH= NC$^{\bullet}$HOOH‡, which is found to spontaneously undergo an extremely exothermic internal reaction resulting in CHONCO (formyl isocyanate) and H$_2$O and in regeneration of the OH radical:

$$HC^{\bullet}=NCH_2OOH + O_2 \rightarrow C≡NCH_2OOH + HO_2$$
$$\Delta H^{\Theta} = -65 \text{ kJ mol}^{-1} \qquad (19a)$$

$$\rightarrow O^{\bullet}OCH=NCH_2OOH^{\ddagger} \quad \Delta H^{\Theta} = -164 \text{ kJ mol}^{-1} \qquad (19b)$$

$$O^{\bullet}OCH=NCH_2OOH^{\ddagger} \rightarrow C≡NCH_2OOH + HO_2$$
$$\Delta H^{\Theta} = +91 \text{ kJ mol}^{-1} \qquad (20a)$$

$$\rightarrow CHONCO + H_2O + OH \quad \Delta H^{\Theta} = -458 \text{ kJ mol}^{-1} \qquad (20b)$$
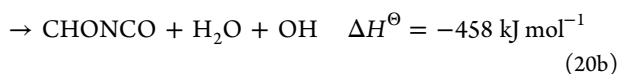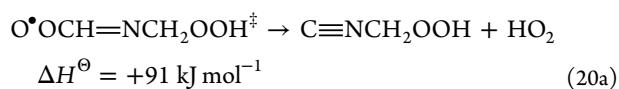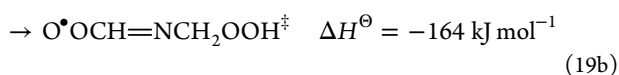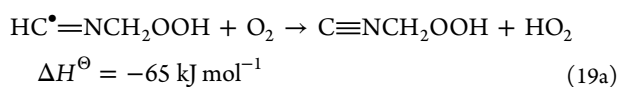
The relative energies of the stationary points on the PESes of reactions 19 and 20 are included in Figure 4 (energies and Cartesian coordinates of the stationary points of the reactions are found in Table S7). Reaction 19a proceeds via a weak prereaction complex, a submerged barrier, and a postreaction HO$_2$ complex; for the sake of legibility, the postreaction complex has been omitted from Figure 4.

The CH$_2$=NC$^{\bullet}$H$_2$ + O$_2$ reaction sequence (16)−(20) was modeled in master equation calculations based on the PES illustrated in Figure 4 and including the peroxy radical removal by NO:
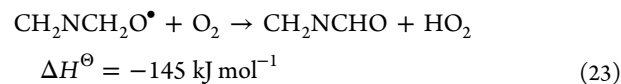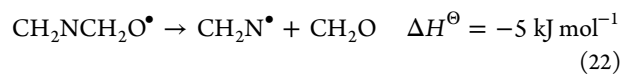
$$CH_2NCH_2OO^{\bullet} + NO \rightarrow CH_2NCH_2O^{\bullet} + NO_2$$
$$\Delta H^{\Theta} = -69 \text{ kJ mol}^{-1} \qquad (21)$$
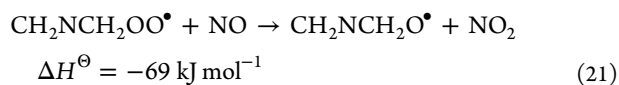
Typical rate coefficients for the R + O$_2$ → RO$_2$ and RO$_2$ + NO → RO + NO$_2$ reactions (5 × 10^{-12} to 10^{-11} cm^3 molecule^{-1} s^{-1} at 298 K[51]) and an NO level of 10 ppbV were employed in modeling the competing reactions. RRKM calculations give a thermal rate coefficient $k_{19a} \approx 3 \times 10^{-14}$ cm^3 molecule^{-1} s^{-1} at 298 K, which is orders of magnitude too slow to compete with reaction 19b. It is also obvious that reaction 20b will be orders of magnitude faster than reaction 20a and that CHONCO therefore will be the by far dominant product (>99.9%) in the HC$^{\bullet}$=NCH$_2$OOH + O$_2$ reaction.

Concerning the branching between routes 17−19 and 21, the master equation calculations forecast a maximum CH$_2$NCH$_2$O$^{\bullet}$ yield of 15% under atmospheric conditions

assuming an NO level of 10 ppb; under chamber conditions with ~50 ppbV NO, the yield could be up to 50%.

The oxy-radical formed in (21) may either dissociate or undergo H-abstraction by O$_2$:

$$CH_2NCH_2O^{\bullet} \rightarrow CH_2N^{\bullet} + CH_2O \quad \Delta H^{\Theta} = -5 \text{ kJ mol}^{-1} \qquad (22)$$

$$CH_2NCH_2O^{\bullet} + O_2 \rightarrow CH_2NCHO + HO_2$$
$$\Delta H^{\Theta} = -145 \text{ kJ mol}^{-1} \qquad (23)$$

The barrier to the N−C scission, reaction 22, is calculated to be well below the entrance energy of reactants in reaction 21, and the fate of the CH$_2$NCH$_2$O$^{\bullet}$ radical will therefore depend on pressure and the energy partitioning in reaction 21. Figure S6 shows the relative energies of the stationary points on the PES of the CH$_2$NCH$_2$OO$^{\bullet}$ + NO reaction; energies and Cartesian coordinates are found in Table S8.

Master equation calculations were carried out to estimate the branching ratio (22):(23) at typical atmospheric conditions. For equipartitioning of the reaction enthalpy in reaction 19 the (22):(23) branching ratio is calculated to be 97:3 under atmospheric pressure and ⟨ΔE_{down}⟩ = 250 cm^{-1}. The fundamental modes of vibration in NO$_2$ are around 750, 1318, and 1618 cm^{-1}. Assuming that the product NO$_2$ has one quantum of the antisymmetric stretching mode (~19 kJ mol^{-1}) and that the remaining reaction enthalpy is equipartitioned, the (22):(23) branching is calculated to be around 50:50. There are no experimental data in the literature on how the energy is distributed in ROO + NO reactions, and the theoretical study thereof can therefore only indicate limits to the atmospheric fate of CH$_2$NCH$_2$O$^{\bullet}$ radicals: >50% HCN + CH$_2$O and <50% CH$_2$=NCHO.

In summary, more than 85% of the CH$_2$NC$^{\bullet}$H$_2$ radicals, formed in H-abstraction from the −CH$_3$ group in MMI, will result in CHONCO, while less than 15% will result in HCN, CH$_2$O, and CH$_2$=NCHO.

3.1.2.4. CH$_3$N=CH$_2$ Reaction with O$_3$. The 1,3-dipolar cycloaddition of ozone to a double bond is challenging to describe accurately in quantum chemistry calculations due to the high multireference character of ozone and the transition states.[52] Nonetheless, Wheeler et al. showed that several multilevel methods perform well for such reactions.[53] We have previously employed the G4 approach to compare the barriers to the O$_3$ reactions with CH$_2$=CH$_2$ and CH$_2$=NH,[20] and we recognized that the HOMO−LUMO gap is more than 100 kJ mol^{-1} larger in the imine than in the corresponding alkene and that this impacts the thermochemistry of all steps in the reaction:

$$CH_3CH=CH_2 + O_3 \rightarrow CH_3\text{-}CH\text{-}CH_2\text{-}OOO^{\ddagger} \quad \Delta H^{\Theta} = -226 \text{ kJ mol}^{-1} \qquad (24)$$

$$CH_3N=CH_2 + O_3 \rightarrow CH_3\text{-}N\text{-}CH_2\text{-}OOO^{\ddagger} \quad \Delta H^{\Theta} = -140 \text{ kJ mol}^{-1} \qquad (25)$$
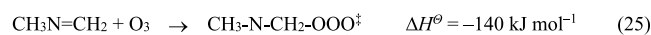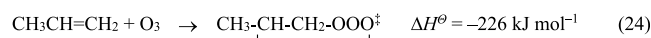
Table S9 compares energies of the stationary points on the PES for the two systems. Both reactions proceed via weak van der Waals complexes and distinctive barriers to formation of the primary ozonides. The barrier to formation of the primary ozonide is significantly higher for MMI ($\Delta E^{\dagger}_{Elec+ZPE}$ = 38.3, $\Delta G^{\dagger}_{298}$ = 87.6 kJ mol^{-1}) than for propene ($\Delta E^{\dagger}_{Elec+ZPE}$ = 15.2, $\Delta G^{\dagger}_{298}$ = 61.9 kJ mol^{-1}). Accordingly, the reactivity toward ozone is obviously lower, and Transition State Theory predicts the rate coefficients to be 1.1 × 10^{-22} cm^3 molecule^{-1} s^{-1} for the CH$_3$N=CH$_2$ + O$_3$ reaction and 3.5 × 10^{-18} cm^3 molecule^{-1} s^{-1} for the CH$_3$CH=CH$_2$ + O$_3$ reaction, for
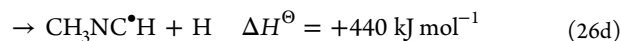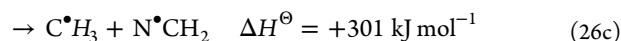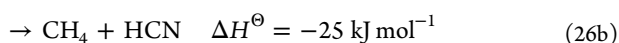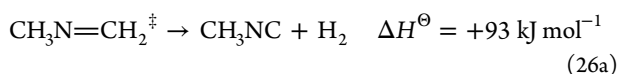
Scheme 1. Major Routes for the OH-Initiated Photo-oxidation of $CH_3N{=}CH_2$ under Atmospheric Conditions as Resulting from Theoretical Calculations[a]
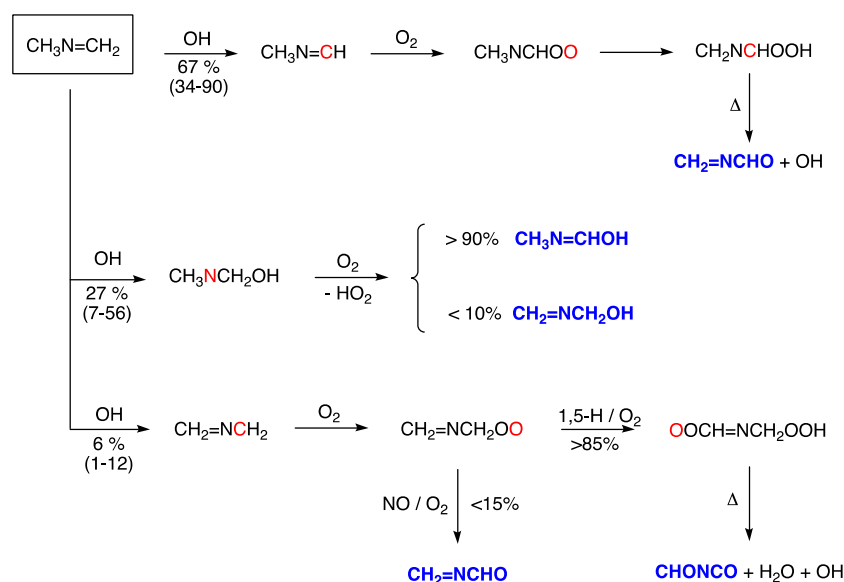
[a]Conservative limits to estimated branchings are given in parentheses; thermally stable products are typeset in bold blue font; radical sites are indicated in red font.

which the recommended rate coefficient is 1.6×10^{-18} cm^3 molecule^{-1} s^{-1} at 1 atm and 298 K.[54] This gives confidence in the computational approach, and even allowing for a significant error in the calculated barrier to the $CH_3N{=}CH_2 + O_3$ reaction, it can be concluded that the reaction is too slow to be of any importance under atmospheric conditions—MMI is "essentially non-reactive toward O$_3$".[15]

3.1.2.5. Tropospheric Photolysis. TDDFT calculations[55] employing the B3LYP functional place the lowest vertical singlet excitation energy in MMI (n → π* transition) at 255 nm with an oscillator strength $f = 0.0005$. The corresponding vertical excitation energy in $CH_2{=}NH$ is calculated at 245 nm with an oscillator strength $f = 0.0019$, which compares well to the experimental observation of a broad and structureless band with a maximum absorption cross section ~4×10^{-19} cm^2 molecule^{-1} near 250 nm.[56] Assuming a Gaussian line profile with 10 nm half-width, the calculated absorption cross sections of both MMI and $CH_2{=}NH$ just about extend into the actinic region with absorption cross sections becoming <10^{-20} cm^2 molecule^{-1} at 290 nm and <10^{-21} cm^2 molecule^{-1} at 310 nm. The actinic flux in the 290–310 nm region is below 10^{14} photons cm^{-2} nm^{-1} for a solar zenith angle $\theta = 0°$,[48] and tropospheric photolysis of MMI can therefore, at best, only be efficient in a very few regions of the Earth.

As in $CH_2{=}NH$,[57] there is conical intersection between the S_0 and S_1 potential surfaces of MMI with the minimum energy crossing point (MECP) located close to the S_1 potential energy minimum. This indicates that an excitation to the S_1 state will be followed by vibrational relaxation and a very rapid radiationless crossing to S_0, where at most 400 kJ mol^{-1} ($\lambda = 300$ nm) then will be available to dissociation processes before collisional quenching establishes thermal equilibrium:

$$CH_3N{=}CH_2^{\ddagger} \rightarrow CH_3NC + H_2 \quad \Delta H^{\ominus} = +93 \text{ kJ mol}^{-1} \tag{26a}$$

$$\rightarrow CH_4 + HCN \quad \Delta H^{\ominus} = -25 \text{ kJ mol}^{-1} \tag{26b}$$

$$\rightarrow C^{\bullet}H_3 + N^{\bullet}CH_2 \quad \Delta H^{\ominus} = +301 \text{ kJ mol}^{-1} \tag{26c}$$

$$\rightarrow CH_3NC^{\bullet}H + H \quad \Delta H^{\ominus} = +440 \text{ kJ mol}^{-1} \tag{26d}$$

There are two routes to H$_2$ elimination (*E*- and *Z*-saddle point configurations) having barriers of 364 and 342 kJ mol^{-1}, respectively; there is no electronic barrier to CN-scission in addition to the endothermicity, and the $CH_4 + HCN$ route is located with a barrier of 340 kJ mol^{-1} (CC//M06-2X results, Table S10). The conceivable tropospheric photolysis processes will therefore be completely dominated by route 26c, where the $N^{\bullet}CH_2$ radical subsequently will undergo H-abstraction by O$_2$ resulting in HCN:

$$N^{\bullet}CH_2 + O_2 \rightarrow HCN + HO_2 \quad \Delta H^{\ominus} = -96 \text{ kJ mol}^{-1} \tag{27}$$
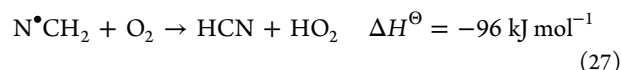
Schade and Crutzen considered route 26a in their reflections on routes to N$_2$O formation in the atmospheric degradation of methylamines.[11] The present results clearly demonstrate that high barriers block this route. In addition, a recent experimental and theoretical study of the atmospheric chemistry CH$_3$NC shows CH$_3$NCO as the only product.[22]

3.1.2.6. Photo-oxidation Mechanism. The theoretically predicted major atmospheric degradation routes of MMI are outlined in Scheme 1 and include the ab initio calculated branching ratios with estimated range limits. The mechanism, originating in quantum chemistry and master equation calculations, displays little resemblance to that proposed by Schade and Crutzen,[11] who did not consider abstraction from the ${=}CH_2$ group, which we find to be a dominant route. The major primary products in atmospheric MMI photo-oxidation are predicted to be other imines: $CH_2{=}NCHO$ (*N*-methyleneformamide) and $CH_3N{=}CHOH$ (*N*-methylformamidic acid). The latter is a tautomer of *N*-methylformamide, but the barrier, being around 135 kJ mol^{-1}, slows tautomerization resulting in a thermal lifetime ~20 d in the gas phase.
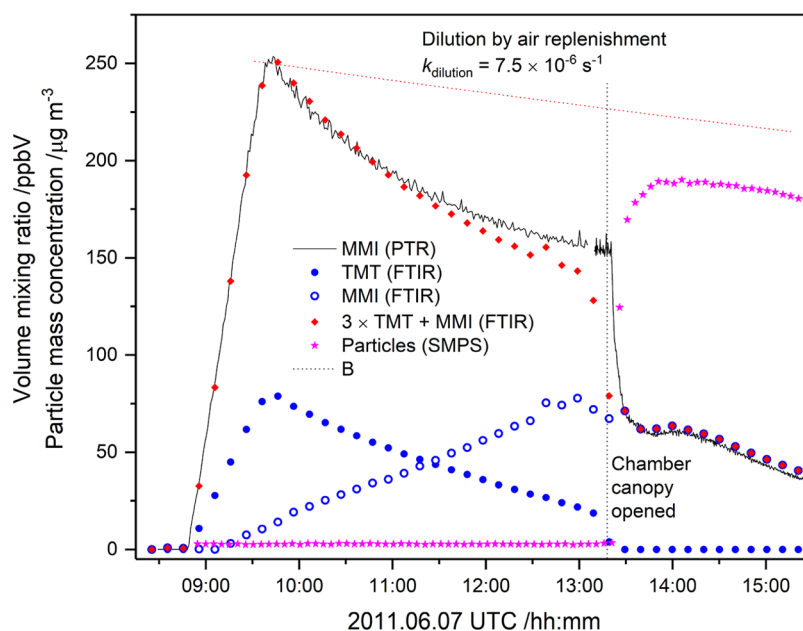
Figure 5. Comparison of 1,3,5-trimethyl-1,3,5-triazinane (TMT) and *N*-methylmethanimine (MMI) volume mixing ratios obtained by PTR-TOF-MS and FTIR, and the temporal particle mass concentration during the 2011.06.07 photo-oxidation experiment in the EUPHORE atmospheric simulation chamber B.
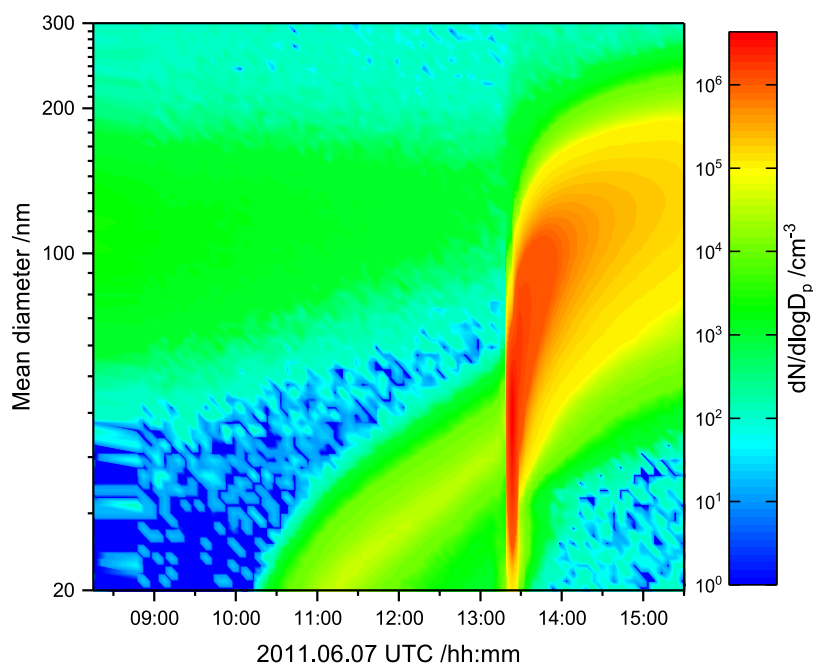

Figure 6. Particle number concentration and particle size distribution from SMPS measurements during the 2011.06.07 photo-oxidation experiment in the EUPHORE atmospheric simulation chamber B.

The predicted photo-oxidation products allow an experimental determination of the branching in reaction 1: CHONCO (formyl isocyanate) is unique to the CH$_3$-abstraction route; CH$_3$N=CHOH and CH$_2$=NCH$_2$OH (methyleneamino-methanol)—having the same sum formula—are unique to the C-addition route; CH$_2$=NCHO (*N*-methyleneformamide) is not unique to the CH$_2$−abstraction route, but for all practical purposes it is, as the contribution from the CH$_3$-abstraction route will be minute.

3.2. Experimental Results. *3.2.1. EUPHORE Experiments.* Six MMI photo-oxidation experiments were carried out in the

200 m^3 EUPHORE atmospheric simulation chamber. The attempts to determine the MMI photo-oxidation products unambiguously were unconvincing due to (1) the slow monomer−trimer equilibration in the simulation chamber, (2) surface reactions, and (3) prominent particle formation. The experiments were, however, not without intellectual value.

TMT was not identified in any chamber experiments by PTR-ToF-MS (C$_6$H$_{16}$N$_3^+$, *m/z* 130.134). This is a natural consequence of the TMT ⇌ 3 MMI equilibrium being strongly temperature dependent ($\Delta H_{exp} \sim 150$,[14] $\Delta G_{calc} = 95$, $\Delta H_{calc} = 177$; all in kJ mol^{-1}), the subppm level TMT
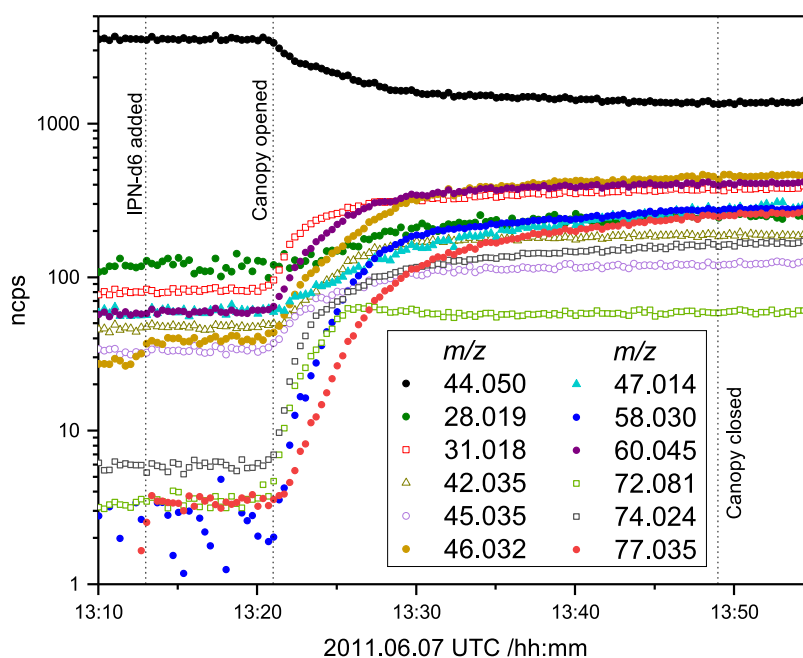
Figure 7. Normalized ion counts registered by PTR-ToF-MS during the 2011.06.07 photo-oxidation experiment in the EUPHORE atmospheric simulation chamber B.

Table 1. Ion Signals Observed in *N*-Methylmethanimine (MMI) and 1,3,5-Trimethyl-1,3,5-triazinane (TMT) Photo-oxidation Experiments[a]

EUPHORE	TMT	MMI	Ion sum formula	Neutral molecule	Interpretation and comments
28.019			CH_2N^+	HCN, HNC	Secondary product
	30.034	30.034	CH_4N^+	$CH_2=NH$	From CH_3NH_2 photo-oxidation
31.019	31.019	31.019	CH_3O^+	CH_2O	From hydrolysis of TMT and/or MMI
	32.050	32.050	CH_6N^+	CH_3NH_2	From hydrolysis of TMT and/or MMI
33.034			CH_5O^+	CH_3OH	Chamber artefact
42.034		42.034	$C_2H_4N^+$		Fragment of $[CH_3N=CHOH]H^+$ and $[CH_2=NCH_2OH]H^+$
44.050	44.050	44.050	$C_2H_6N^+$	$CH_3N=CH_2$	MMI
45.034			$C_2H_5O^+$	CH_3CHO	Chamber artefact?
46.029			CH_4NO^+	NH_2CHO	From hydrolysis of $CH_2=NCHO$?
47.013			$CH_3O_2^+$	HCOOH	Artefact or hydrolysis of $CH_3N=CHOH$
58.029	58.029	58.029	$C_2H_4NO^+$	$CH_2=NCHO$	Product from CH_2-abstraction in MMI and CH_3-abstraction in TMT
				CH_3NCO	Product from CH_2-abstraction in TMT
60.045		60.045	$C_2H_6NO^+$	$CH_2=NCH_2OH$	Products from MMI C-addition reaction.
				$CH_3N=CHOH$	
61.029			$C_2H_5O_2^+$	CH_3COOH	Chamber artefact
72.045			$C_3H_6NO^+$		Condensation product ?
72.081			$C_4H_{10}N^+$		Condensation product ?
74.024			$C_2H_4NO_2^+$		$CHON=CHOH$ or $CHONHCHO$?
77.035	77.035	77.035	$CH_5N_2O_2^+$	CH_3NHNO_2	From CH_3NH_2 photo-oxidation

Table column header: m/z — EUPHORE, Oslo (TMT, MMI)

[a]Only ion signals having an intensity >1% of the decrease in the MMI signal m/z 44.050 during the time of reaction are included in the table. Fragment ions, ^{13}C-containing ions, instrument-intrinsic ions, and ions arising from side reactions are not included.

concentrations in the experiments and the surface temperatures of the PTR instrument inlet and detection system; an initial 1 ppm V TMT will equilibrate to ~30% trimer at room temperature; at 75 °C the equilibrium is shifted to <0.1% TMT.

Figure 5 compares the time profiles of MMI and TMT independently obtained by FTIR and PTR-ToF-MS (protonated MMI, $C_2H_6N^+$, m/z 44.050) during an EUPHORE experiment. In this particular experiment, 170 mg TMT was injected in an airstream to the chamber and left for nearly 4 h before the OH precursor IPN-d6 was added and the chamber

canopy opened to sunlight ($(CD_3)_2CHONO + h\nu \rightarrow (CD_3)_2CHO^\bullet + NO$; $(CD_3)_2CHO^\bullet + O_2 \rightarrow (CD_3)_2CO + HO_2$; $HO_2 + NO \rightarrow OH + NO_2$). During this period the SMPS (Scanning Mobility Particle Sizer) showed only a minute gas-to-particle transfer, while the FTIR showed around 75% reduction in TMT and a less than stoichiometric increase in MMI. That is, an appreciable amount of TMT and/or MMI was lost to the chamber walls before the photo-oxidation was initiated by opening the chamber canopy. This is also reflected in the PTR-TOF-MS signal that correlates well with the sum MMI + 3 × TMT from FTIR; the temporal MMI signal shows
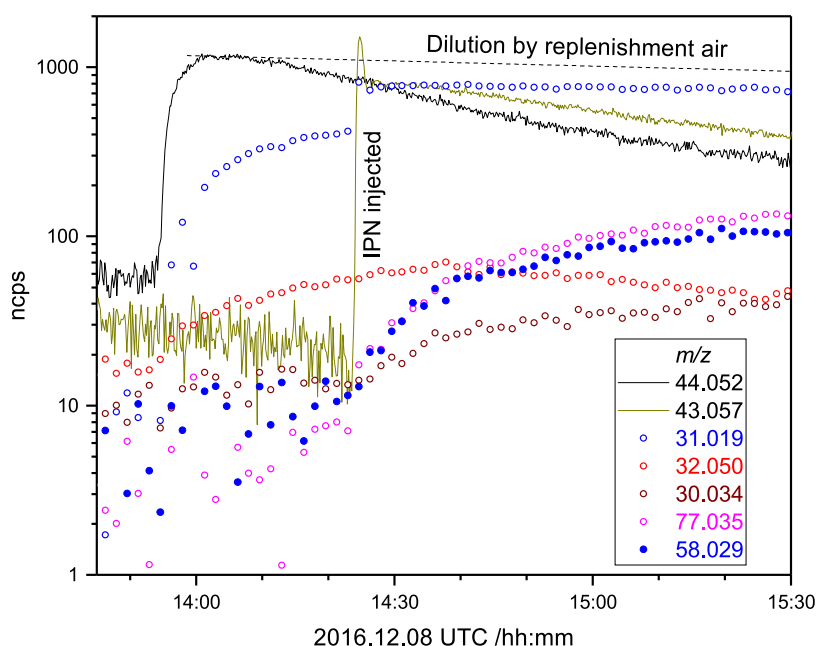
Figure 8. Normalized ion counts registered during the high-NOx 1,3,5-trimethyl-1,3,5-triazinane (TMT) photo-oxidation experiment on 2016.12.08. Signals: m/z 44.052 ($C_2H_6N^+$, protonated $CH_3N{=}CH_2$), 43.057 ($C_3H_7^+$, fragment of IPN), 31.019 (CH_3O^+, protonated CH_2O), 32.050 (CH_6N^+, protonated CH_3NH_2), 30.034 (CH_4N^+, protonated $CH_2{=}NH$), 77.035 ($CH_5N_2O_2^+$, protonated CH_3NHNO_2), and 58.029 ($C_2H_4NO^+$, protonated CH_3NCO and/or $CH_2{=}NCHO$).

an exponential decay with a rate of 3.5×10^{-5} s^{-1}, which is around 5 times larger than the chamber dilution by replenishment air.

TMT is a tertiary (cyclic) triamine and is therefore expected to react very fast with OH radicals, $k_{\text{TMT+OH}} > 5 \times 10^{-11}$ cm^3 molecule^{-1} s^{-1}.[9] When the chamber canopy was opened to solar radiation (~13:20 UTC, Figure 5), the remaining gas phase TMT reacted within 20 min, whereas the MMI showed a more sedate decay. Figure 5 also includes the SMPS results for the total particle mass concentration during the experiment, while Figure 6 shows the particle number concentration and particle size distribution. It can be seen that the very fast TMT loss is paralleled by a steep increase in particle mass concentration to around 175 μg m^{-3}, which hypothetically corresponds to ~25 ppb TMT being transferred from the gas to the particle phase as 1:1 TMT:HNO$_3$ salt. MMI, being a strong base, will also transfer to the particle phase. However, Figure 5 suggests that only a small amount of MMI is transferred to the particles in the initial phase of the photo-oxidation experiment.

The temporal PTR-ToF-MS ion signals observed in the 2011.06.07 experiment are illustrated in Figure 7, and the PTR-MS results from the six experiments are summarized in Table 1 containing ion signals having an intensity >1% of the decrease in the TMT/MMI signal m/z 40.050 during the time the chamber canopy was open. It is emphasized that there are no indications of the nitrosamine, $CH_3N(NO)CH_2OH$, or of the nitramine, $CH_3N(NO_2)CH_2OH$, which potentially could result in the photo-oxidation of MMI; see section 3.1.2.1. It should also be noted that particles to some degree can evaporate in the heated sampling lines and, in particular, in the drift tube of the PTR-MS analyzer.[58] Some of the ion signals reported in Table 1 and Figure 7 may therefore, at least in part, have their origin in the particle phase.

The ion signals can be divided into two main groups: (1) m/z 31.019, 33.034, 42.034, 46.029, and 72.081 that are distinctly correlated with TMT before opening the chamber canopy and anticorrelated after; (2) m/z 45.034, 58.029, 72.045, and 77.035 that only increase after opening the chamber canopy. The most striking signal is that of m/z 77.035 ($CH_5N_2O_2^+$), which will be addressed later. The m/z 28.019 (CH_2N^+) is burdened by a high background, but has the temporal profile of a secondary product. Finally, the m/z 72.081 ($C_4H_{10}N^+$) has distinct temporal signal profile in all experiments and is clearly the result of heterogeneous processing. In conclusion, most of the ion signals observed in the EUPHORE experiments likely have several origins making mechanistic deductions irrational.

3.2.2. Oslo Smog Chamber Experiments. A series of low concentration experiments were carried out in the Oslo stainless steel reactor to establish a distinction between products from TMT and from MMI photo-oxidation and various artifacts related to possible surface and particle reactions. The disadvantage of metallic surfaces in relation to bases like MMI and TMT is to some extent countered by ease of cleansing the walls, interfacing preparative equipment, and selection of photolysis light sources.

Low concentration TMT photo-oxidation experiments were performed by first injecting TMT into the 350−400 nm irradiated chamber followed by injecting the OH precursor IPN. Figure 8 illustrates the results of an experiment in which TMT was administered to the chamber to around 25 ppbV in clean air, from which it can be seen that there is the foreseeable, extensive loss of TMT to the chamber walls, making quantification of yields futile.

The expected primary photo-oxidation products of TMT (1,3,5-trimethyl-1,3,5-triazinen-2-one, TMTCO, and 3,5-trimethyl-1,3,5-triazinena-1-carbaldehyde, TMTCHO, see Scheme S1) are in equilibrium with their monomeric constituents TMTCO $\rightleftarrows$ 2MMI + CH_3NCO ($\Delta G_{\text{TMTCO,calc}}$ = 92, $\Delta H_{\text{TMTCO,calc}}$ = 209 kJ mol^{-1}) and TMTCHO $\rightleftarrows$ 2MMI + $CH_2{=}NCHO$ ($\Delta G_{\text{TMTCHO,calc}}$ = 111, $\Delta H_{\text{TMTCHO,calc}}$ = 228 kJ mol^{-1}). Like TMT, neither TMTCO nor TMTCHO were
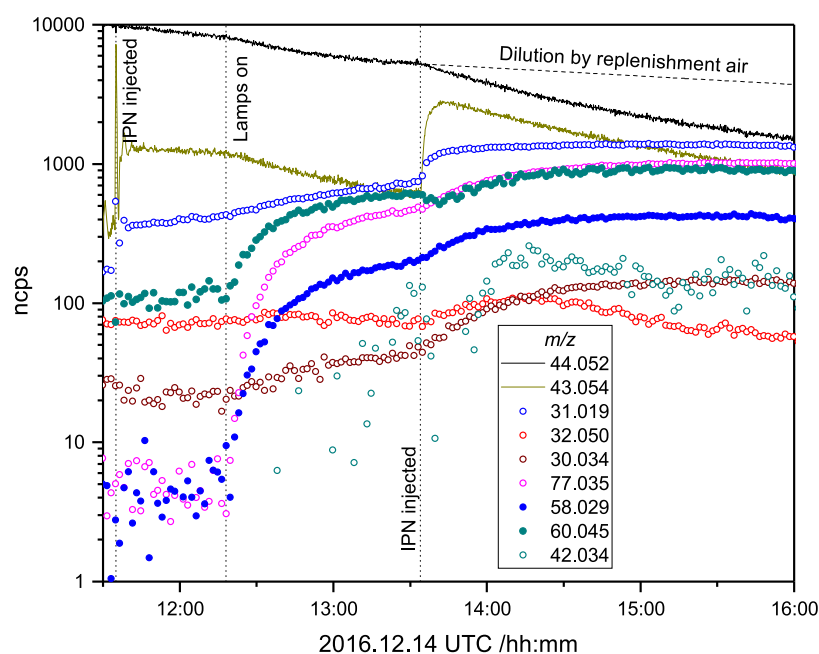
Figure 9. Normalized ion counts registered during the *N*-methylmethanimine (MMI) photo-oxidation experiment on 2016.12.14. Signals: m/z 44.052 ($C_2H_6N^+$, protonated $CH_3N=CH_2$), 43.054 ($C_3H_7^+$, fragment of IPN), 31.019 (CH_3O^+, protonated CH_2O), 32.050 (CH_6N^+, protonated CH_3NH_2), 30.034 (CH_4N^+, protonated $CH_2=NH$), 77.035 ($CH_5N_2O_2^+$, protonated CH_3NHNO_2), 58.029 ($C_2H_4NO^+$, protonated CH_3NCO and/or $CH_2=NCHO$), 60.045 ($C_2H_6NO^+$, protonated $CH_3N=CHOH$ and/or $CH_2=NCH_2OH$), and 42.034 ($C_2H_4N^+$, fragment of protonated $CH_3N=CHOH$ and/or $CH_2=NCH_2OH$).

detected directly by the PTR-ToF-MS instrument employed; in fact, no relevant ion signals above m/z 78 were detected in any experiment.

In addition to ion signals related to IPN and TMT, only five ion signals above 10 normalized counts per second (ncps) were observed with temporal profiles correlated to the injections: (1) m/z 32.050 (CH_6N^+) and 31.018 (CH_3O^+) that both started to grow as soon as TMT was injected and (2) m/z 30.034 (CH_4N^+), 77.035 ($CH_5N_2O_2^+$), and 58.029 ($C_2H_4NO^+$) that started to grow when IPN was injected, Figure 8. The group 1 ion signals are recognized as protonated CH_3NH_2 and CH_2O that are formed by hydrolysis of TMT on the chamber surfaces; later, photo-oxidation of IPN also contributes to the m/z 31.018 ion signal. The group 2 signals m/z 30.034 and 77.035 are familiar from CH_3NH_2 photo-oxidation experiments and relate to protonated $CH_2=NH$ and CH_3NHNO_2.[4] Finally, the m/z 58.029 is interpreted as protonated CH_3NCO and/or $CH_2=NCHO$—the two monomeric components of the expected primary TMT photo-oxidation products TMTCO and TMTCHO.

The MMI photo-oxidation experiments were performed by directing heated TMT/MMI vapor via dry ice traps directly into the evacuated chamber, which was then filled with clean air to atmospheric pressure before adding IPN and turning the photolysis lamps on. Figure 9 illustrates the PTR results from an experiment in which MMI was added to the chamber to achieve a mixing ratio of around 500 ppb (quantified by both FTIR and PTR). It is highly important that the FTIR spectra recorded during the experiment illustrated do not show any spectral features attributable to TMT. Again, it is emphasized that there are no indications of the nitrosamine, $CH_3N(NO)$-CH_2OH, or of the nitramine, $CH_3N(NO_2)CH_2OH$, which potentially could result in the photo-oxidation of MMI.

As in the TMT experiments, there is a clear loss of MMI to the chamber walls, making it difficult to assess mass balance in

the experiment; the MMI wall loss is apparently roughly at the same level as the dilution by air replenishment. This is also evidenced by the visibly reduced CH_2O and CH_3NH_2 formation from MMI hydrolysis.

Only two ion signals above 10 ncps were detected in addition to the ones observed in the "pure" TMT experiments: m/z 60.049 ($C_2H_6NO^+$) and 42.034 ($C_2H_4N^+$). The former signal, corrected for isotope interference from IPN and acetone, is interpreted as protonated $CH_3N=CHOH$ and/or $CH_2=NCH_2OH$ − the photo-oxidation product(s) resulting from OH addition to the π-system carbon atom, Scheme 1. The latter weak and noisy signal is understood as the corresponding two dehydration fragments ($CH_3N=CH^+$ and $CH_2=NCH_2^+$). The m/z 58.033 is interpreted as protonated $CH_2=NCHO$ − the major photo-oxidation product following H-abstraction from the CH_2 group in MMI. $CH_2=NCHO$ is also predicted as a minor product resulting from H-abstraction from the CH_3-group (<15%). There is, however, no obvious ion signal from the major product following H-abstraction from the CH_3-group, CHONCO at m/z 72.009, indicating that the yield of this route is either very small or that CHONCO reacts very fast with OH. A recent study of the CH_3NCO + OH reaction shows CHONCO as the primary product,[59] and a comparison of the published CH_3NCO and CHONCO time profiles (Figure 7 in ref 59) indicates that CHONCO reacts around 20 times faster with OH than the parent compound, $k_{OH+CH3NCO} = 1.36 \times 10^{-13}$ cm^3 molecule^{-1} s^{-1} at 298 K.[59] This places the OH-reactivity of CHONCO on the same scale as that of MMI, which, in turn, implies that CHONCO should be a reliable indicator of H-abstraction from the CH_3-group. While the m/z 72.008 intensity is well below the 1% cutoff limit, it can safely be concluded that the CH_3-abstraction route in the MMI + OH reactions amounts to <2%.

Because the FTIR spectra unambiguously show that TMT is not present in any significant amount in this experiment, the
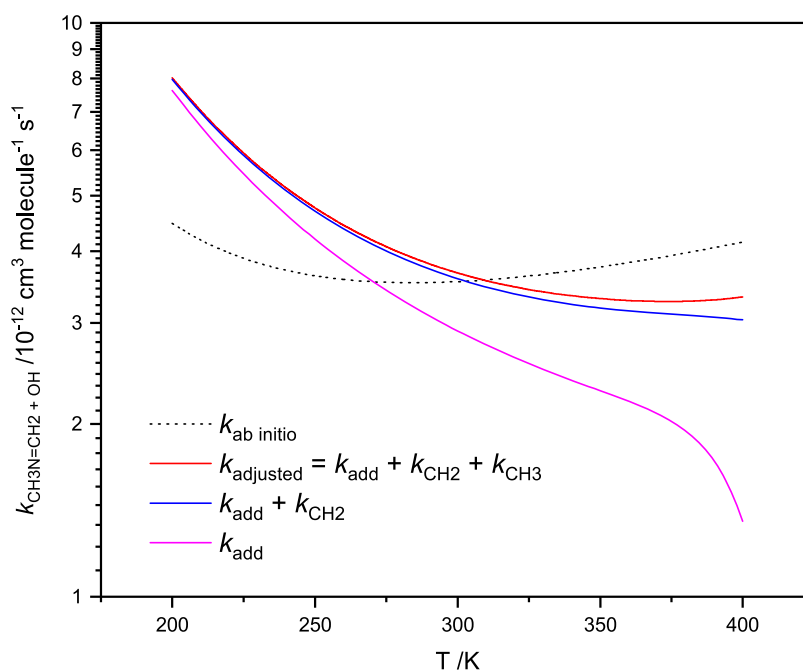
Figure 10. Cumulative plot of rate coefficients for the OH radical reaction with *N*-methyl methanimine calculated with Eckart tunneling, hindered internal rotations, scaled vibrational wavenumbers, and adjusted barrier heights to reproduce the observed branching in the reaction. Based on results from CCSD(T*)-F12a/aug-cc-pVTZ//M06-2X/aug-cc-pVTZ calculations.
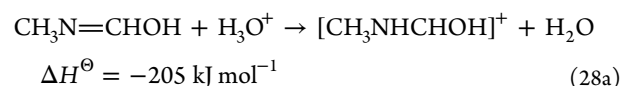
relative ion signal intensities between *m/z* 58.029 and the sum of 60.045 and 42.034 reflect the branching between H-abstraction from the $=CH_2$ group and C-addition in the MMI + OH reaction.

The relative instrument sensitivity to $CH_2=NCH_2OH$, $CH_3N=CHOH$, and $CH_2=NCHO$ essentially only depends the ion−molecule reaction rate coefficients, since the instrumental mass discrimination function is effectively the same for *m/z* 58.029 and 60.045 and since ionization in PTR-MS happens at the collisional rate.[60] The ion−molecule reaction rate coefficients, in turn, can be quite precisely estimated from the calculated dipole moments and isotropic polarizabilities listed in Table S1.[30] For *E/N* 107 Td, the following rate coefficients are calculated: $k_{CH2=NCH2OH+H3O+} =$ 2.28, $k_{CH3N=CHOH+H3O+} = 1.69$, and $k_{CH2=NCHO+H3O+} = 3.06 \times 10^{-9}$ cm^3 molecule^{-1} s^{-1} at a drift tube temperature of 100 °C. The *m/z* 58.029 and 60.045 ion signals are excellently correlated throughout the experiment, except in the short period when IPN was injected. An analysis of the time periods 12:30−13:30 and 13:45−16:00, based upon the above-mentioned ion−molecule reaction rate coefficients and a 90:10 ratio in the $CH_3N=CHOH : CH_2=NCH_2OH$ product distribution of the OH addition route, finds the branching ratio between H-abstraction from the CH_2 group and C-addition to be 18:82 ± 3 (3σ-limit). Changing the theoretical value for the $CH_3N=CHOH:CH_2=NCH_2OH$ product distribution in the addition route from 90:10 to 70:30 or 100:0 only alters the derived branching within the estimated error limits.

3.3. Synthesis of Experimental and Theoretical Results. The present quantum chemistry calculations are not capable of narrowing the branching in the MMI + OH reaction better than 34−90% CH_2−abstraction, 7−56% C-addition, and 1−12% CH_3-abstraction, Scheme 1. In principle, the three routes can be discerned by PTR-MS as the major product of each route has a different mass. The PTR-MS results place a clear upper limit of 2% to the CH_3-abstraction

route and an 18:82 ± 3 ratio between CH_2 abstraction and C-addition. The experimental value assumes (1) that no tautomerization of the MMI + OH reaction products occurs in the instrument inlet lines and detection system and (2) that the dehydration of protonated $CH_3N=CHOH$ and $CH_2=NCH_2OH$ takes place.

The fragmentation of protonated $CH_3N=CHOH$ and $CH_2=NCH_2OH$ was investigated in theoretical calculations showing that proton transfer selectively takes place at the OH-group and that $CH_2=NCH_2OH_2^+$ spontaneously ejects H_2O, resulting in the $[CH_2=N=CH_2]^+$ cation. The proton transfer in the $CH_3N=CHOH + H_3O^+$ reaction is more complex, taking place via complex formation on the entrance side followed by competing H-migration and H_2O ejection. There is a relatively low barrier of 27 kJ mol^{-1} between the H_3O^+ complex on the entrance side and the post transfer dimeric H_2O complex on the exit side and a somewhat larger barrier of 67 kJ mol^{-1} to the H-migration route.

$$CH_3N=CHOH + H_3O^+ \rightarrow [CH_3NHCHOH]^+ + H_2O$$

$$\Delta H^\Theta = -205 \text{ kJ mol}^{-1} \tag{28a}$$

$$\rightarrow [CH_3NCH]^+ + 2H_2O \quad \Delta H^\Theta = -51 \text{ kJ mol}^{-1} \tag{28b}$$

The energetics of reaction 28 is illustrated in Figure S7 (the underlying quantum chemistry results are documented in Table S11). The branching in reaction 28 was investigated in master equation calculations based on the PES illustrated in Figure S7; the effective temperature in the PTR-ToF-MS drift tube being operated at *E/N* 88 Td (EUPHORE experiments) is ∼1000 K, whereas the 107 Td employed in the Oslo experiments corresponds to ∼1300 K. The calculations indicate the branching to be determined in part by thermodynamics, and predict a branching of 75:25 at 1000 K and 90:10 at 1300 K, which is consistent with higher relative ion signals of *m/z* 42.034 to 60.045 in the EUPHORE

experiments, Figure 7, than in the Oslo experiments, Figure 9. The branching in the $CH_3N^\bullet CH_2OH + O_2$ reaction (3) can be extracted from the observed relative intensities of the m/z 42.034 and 60.045 ion signals in the Oslo experiments when taking the calculated fragmentations of protonated CH_3N=CHOH (10%) and CH_2=NCH_2OH (100%) into consideration. The average m/z 42.034 and 60.045 ion signal ratio 0.42 ± 0.11 corresponds to a branching (3a):(3b) = 22:78 (±10, 2σ). By providence, this compares well with the theoretical result 10:90.

Concerning CH_3N=CHOH → CH_3NHCHO tautomerization, the theoretical study located a barrier around 135 kJ mol^{-1} corresponding to a unimolecular rate coefficient around 1.4×10^{-6} s^{-1} at 298 K and 2.7×10^{-4} s^{-1} at 398 K. Consequently, CH_3N=CHOH is not expected to tautomerize to any significant degree in the PTR inlet and detection system unless the process is surface catalyzed. In the hypothetical case of 100% tautomerization of CH_3N=CHOH to CH_3NHCHO, the instrument response factor for m/z 60.045 should then be based on $k_{CH3NHCHO+H3O+} = 4.12 \times 10^{-9}$ cm^3 molecule^{-1} s^{-1} at 100 °C. This, in turn, would bring the estimated branching ratio between H-abstraction from the CH_2 group and C-addition to be 34:66 ± 3 (3σ-limit). In any case, there is an obvious discord between theory and experiments with respect to the initial branching in the MMI + OH reaction.

The sensitivity analysis of the quantum chemistry based kinetic model for the MMI + OH reaction shows that the reaction rate coefficient and the branching essentially only depend on the saddle point energies SP-1a (C-addition) and SP-1c (CH_2-abstraction leading to E-CH_3N=CH). We consider the calculated saddle point energies associated with uncertainties of ±4 kJ mol^{-1}. It is, however, not possible to reproduce the observed branching by adjusting a single saddle point energy by only 4 kJ mol^{-1}. As there is no unique solution to fitting the experimental branching by adjusting the saddle point energies, we therefore advocate a single correction as a first approach: $-\Delta E$ to the C-addition saddle point energy (SP-1a) and $+\Delta E$ to each of the three saddle points to H-abstraction (SP-1c, SP-1d, and SP-1e). Adjusting the saddle point energies as indicated above by $\Delta E = 3.15$ kJ mol^{-1} changes the branching between reactions 1a−1e from 27:0:64:3:6 to 80:0:1:17:2 while leaving the calculated rate coefficient at 298 K essentially unchanged. Figure 10 compares the ab initio and the adjusted ab initio rate coefficients for the overall CH_3N=CH_2 + OH reaction as a function of temperature. The difference between the two predictions is surprisingly small—less than a factor of 2 for tropospheric conditions. The figure also illustrates the contribution from the addition and the CH_2-abstraction routes to the total rate coefficient (the rate coefficients for the individual routes are documented in Table S12 for selected temperatures). The overall rate coefficient shows a moderate pressure dependency under tropospheric conditions (100−1000 mbar, 220−300 K) with a variation of ~15% at 220 K, Figure 11. Discrete values of $k(p,T)$ are collected in Table S13.

The temperature dependence of the rate coefficient at 1000 mbar can conveniently be parametrized according to the modified Arrhenius equation $k(T) = 5.70 \times 10^{-14} \times (T/298$ K$)^{3.18} \times \exp(1245$ K$/T)$ cm^3 molecule^{-1} s^{-1} with $k(298$ K$) = 3.7 \times 10^{-12}$ cm^3 molecule^{-1} s^{-1}. The rate coefficient at 298 K is comparable to that of the CH_2=NH + OH reaction, calculated in a similar way $(3 \times 10^{-12}$ cm^3 molecule^{-1} $s^{-1})$,[20] and it is almost an order of magnitude smaller than the
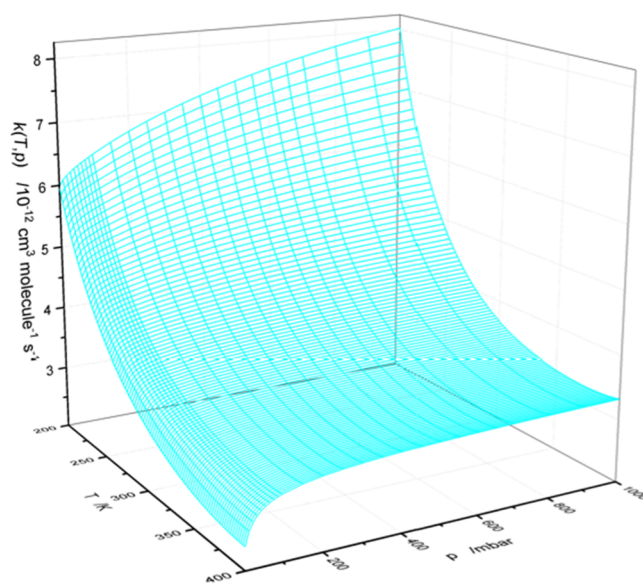
Figure 11. Rate coefficient for the CH_3N=CH_2 + OH reaction as a function of p and T. Results from MESMER calculations including Eckart tunneling and hindered internal rotations, based on CCSD-(T*)-F12a/aug-cc-pVTZ//M06-2X/aug-cc-pVTZ calculations.

recommended high-pressure value for the CH_3CH=CH_2 reaction with OH.[47] In this context, it should be noted that the CH_3CH=CH_2 + OH reaction is entirely an addition reaction under atmospheric conditions, whereas the CH_3N=CH_2 + OH reaction—like the CH_2=NH + OH reaction[20,21]—also proceeds via H−abstraction.

4. CONCLUSIONS

The atmospheric photo-oxidation of MMI $(CH_3N$=$CH_2)$ has been detailed on the basis of quantum chemistry calculations showing CH_2=NCHO and CH_3N=CHOH and/or CH_2=NCH_2OH as the major products; N_2O will not be formed in the atmospheric gas phase degradation, and there are no indications of nitrosamine and nitramine formation. The potential energy surface of the CH_3N=CH_2 + OH reaction was characterized in coupled cluster theory calculations, and master equation modeling reveals a minor pressure dependency and a negative temperature dependency of the reaction, with typical values of k_{OH} around 3.7×10^{-12} cm^3 molecule^{-1} s^{-1} under tropospheric conditions. The MMI + Cl reaction[17] and the MMI + O_3 reaction as well as tropospheric photolysis are all found to be too slow to be of importance on a global scale. With a diurnal OH radical concentration of 10^6 cm^{-3},[61] the atmospheric lifetime of MMI with respect to reaction with OH will be around $2\frac{1}{2}$ days. The night-time chemistry of MMI is likely dominated by the NO_3 radical, and assuming that MMI follows the OH-NO_3 reactivity correlation for either addition or abstraction,[49] this places $k_{NO3+MMI}$ in the range 4.4 $\times 10^{-17}$ to 1.1×10^{-16} cm^3 molecule^{-1} s^{-1} at 298 K. Taking an average night-time NO_3 concentration around 5×10^8 cm^{-3},[49,62] results in $\tau_{NO3} > \frac{1}{2}$ yr for MMI. That is, the NO_3 radical is not expected to present any significant atmospheric sink for MMI.

Urban clouds, fog, and deliquescent particles are in general acidic, and considering the uptake coefficients for methylamines on 59−82 wt % sulfuric acid $(\gamma \sim 2 \times 10^{-2})$[63] as the expected level for imine uptake on particles, in general, the aqueous particle uptake of MMI will be diffusion controlled

under atmospheric conditions. MMI will consequently partition preferentially to the aqueous particle phase,[64] and although atmospheric conditions are highly variable, hydrolysis to CH_2O and CH_3NH_2 will be a dominating atmospheric removal of MMI.

The major MMI photo-oxidation products, $CH_2=NCHO$ and $CH_3N=CHOH$ and/or $CH_2=NCH_2OH$, are likewise expected to partition to the aqueous particle phase where hydrolysis will result in $CH_2O + NH_2CHO$ and $CH_3NH_2 + HCOOH$ or $CH_2O + NH_2CH_2OH$.

■ ASSOCIATED CONTENT

ⓈI Supporting Information

The Supporting Information is available free of charge at https://pubs.acs.org/doi/10.1021/acs.jpca.2c01925.

Infrared spectrum of 1,3,5-trimethylhexahydro-1,3,5-triazine (Figure S1), infrared spectra of a trimerizing $CH_3N=CH_2$ sample (Figure S2), infrared spectrum of $CH_3N=CH_2$ (Figure S3), dipole moments and isotropic polarizabilities (Table S1), quantum chemistry calculation results for the $CH_3N=CH_2 + OH$ reaction (Table S2), OH rotational potentials in the $CH_3N=CH_2+OH$ reaction saddle points (Figure S4), sensitivity analysis of the $CH_3N=CH_2 + OH$ reaction model (Table S3), quantum chemistry calculation results for $CH_3N^\bullet CH_2OH$ formation and isomerization (Table S4), quantum chemistry calculation results for the $CH_3N^\bullet CH_2OH + O_2$ reaction (Table S5), rotational potential of the $CNOO^\bullet$ moiety in the $CH_3N(OO^\bullet)$-CH_2OH radical (Figure S5), quantum chemistry calculation results for the $(E)-CH_3NC^\bullet H + O_2$ reaction (Table S6), quantum chemistry calculation results for the $CH_2NC^\bullet H_2 + O_2$ reaction (Table S7), relative energies of stationary points on the PES of the $CH_2=NCH_2OO^\bullet + NO$ reaction (Figure S6), quantum chemistry calculation results for the $CH_2NCH_2OO^\bullet + NO$ reaction (Table S8), G4 results for the $CH_3CH=CH_2 + O_3$ and $CH_3N=CH_2 + O_3$ reactions (Table S9), quantum chemistry calculation results for CH_3NCH_2 photolysis (Table S10), primary products in the OH initiated photo-oxidation of TMT under atmospheric conditions (Scheme S1), relative energies of stationary points on the PES of the $CH_3N=CCHOH + H_3O^+$ reaction (Figure S7), quantum chemistry calculation results for the $CH_3N=CCHOH + H_3O^+$ reaction (Table S11), calculated rate coefficients for the $CH_3N=CH_2 + OH$ reaction (Table S12), rate coefficients for the $CH_3N=CH_2 + OH$ reaction at discrete values of p and T (Table S13) (PDF)

■ AUTHOR INFORMATION

Corresponding Authors

Claus J. Nielsen − *Section of Environmental Sciences, Department of Chemistry, University of Oslo, 0315 Oslo, Norway;* ⓞ orcid.org/0000-0002-2962-2634; Phone: +47-22855680; Email: c.j.nielsen@kjemi.uio.no

Arne Joakim C. Bunkan − *Section of Environmental Sciences, Department of Chemistry, University of Oslo, 0315 Oslo, Norway;* Present Address: Norwegian Defence Research Establishment (FFI), P.O. Box 25, NO-2027 Kjeller, Norway; ⓞ orcid.org/0000-0002-8923-2603; Email: arne.bunkan@ffi.no

Authors

Nina G. Reijrink − *Section of Environmental Sciences, Department of Chemistry, University of Oslo, 0315 Oslo, Norway;* Present Address: IMT Nord Europe, Institut Mines-Télécom, Univ. Lille, Center for Energy and Environment, F-59000 Lille, France, and Atmospheric Chemistry Department, Max Planck Institute for Chemistry, 55128 Mainz, Germany. Email: n.reijrink@mpic.de

Tomáš Mikoviny − *Section of Environmental Sciences, Department of Chemistry, University of Oslo, 0315 Oslo, Norway*

Markus Müller − *Institute for Ion Physics and Applied Physics, University of Innsbruck, 6020 Innsbruck, Austria;* Present Address: IONICON Analytik GmbH, Eduard-Bodem-Gasse 3, 6020 Innsbruck, Austria. Email: markus.mueller@ionicon.com

Liang Zhu − *Section of Environmental Sciences, Department of Chemistry, University of Oslo, 0315 Oslo, Norway;* Present Address: TOFWERK China, No.320, PuBin Road, Pukou, NanJing, China. Email: liang.zhu@tofwerk.com

Armin Wisthaler − *Section of Environmental Sciences, Department of Chemistry, University of Oslo, 0315 Oslo, Norway; Institute for Ion Physics and Applied Physics, University of Innsbruck, 6020 Innsbruck, Austria;* ⓞ orcid.org/0000-0001-5050-3018

Complete contact information is available at:
https://pubs.acs.org/10.1021/acs.jpca.2c01925

Author Contributions

The manuscript was written through contributions of all authors. All authors have given approval to the final version of the manuscript.

Notes

The authors declare no competing financial interest.

■ ACKNOWLEDGMENTS

■ REFERENCES

(1) Lindley, C. R. C.; Calvert, J. G.; Shaw, J. H. Rate Studies of the Reactions of the $(CH_3)_2N$ Radical with O_2, NO, and NO_2. *Chem. Phys. Lett.* **1979**, *67*, 57−62.

(2) Nielsen, C. J.; D'Anna, B.; Dye, C.; George, C.; Graus, M.; Hansel, A.; Karl, M.; King, S.; Musabila, M.; Müller, M., et al. *Atmospheric Degradation of Amines (ADA). Summary Report: Gas phase photo-oxidation of 2-aminoethanol (MEA)*; NILU: 2010; NILU OR 8/2010.

(3) Nielsen, C. J.; D'Anna, B.; Dye, C.; Graus, M.; Karl, M.; King, S.; Maguto, M. M.; Muller, M.; Schmidbauer, N.; Stenstroem, Y.; et al. Atmospheric Chemistry of 2-Aminoethanol (MEA). *Energy Procedia* **2011**, *4*, 2245−2252.

(4) Nielsen, C. J.; D'Anna, B.; Karl, M.; Aursnes, M.; Boreave, A.; Bossi, R.; Bunkan, A. J. C.; Glasius, M.; Hansen, A.-M. K.; Hallquist,

M., et al. *Summary Report: Photo-oxidation of Methylamine, Dimethyl-amine and Trimetahylamine*. Climit project No. 201604; NILU: 2011; NILU OR 2/2011.

(5) Nielsen, C. J.; D'Anna, B.; Bossi, R.; Bunkan, A. J. C.; Dithmer, L.; Glasius, M.; Hallquist, M.; Hansen, A. M. K.; Lutz, A.; Salo, K., et al. *Atmospheric Degradation of Amines (ADA)*; University of Oslo: Oslo, 2012; http://urn.nb.no/URN:NBN:no-30510.

(6) Tan, W.; Zhu, L.; Mikoviny, T.; Nielsen, C. J.; Wisthaler, A.; Eichler, P.; Müller, M.; D'Anna, B.; Farren, N. J.; Hamilton, J. F.; et al. Theoretical and Experimental Study on the Reaction of tert-Butylamine with OH Radicals in the Atmosphere. *J. Phys. Chem. A* **2018**, *122*, 4470−4480.

(7) Tan, W.; Zhu, L.; Mikoviny, T.; Nielsen, C. J.; Wisthaler, A.; D'Anna, B.; Antonsen, S.; Stenstrøm, Y.; Farren, N. J.; Hamilton, J. F.; et al. Experimental and Theoretical Study of the OH-Initiated Degradation of Piperazine under Simulated Atmospheric Conditions. *J. Phys. Chem. A* **2021**, *125*, 411−422.

(8) Tan, W.; Zhu, L.; Mikoviny, T.; Nielsen, C. J.; Tang, Y.; Wisthaler, A.; Eichler, P.; Müller, M.; D'Anna, B.; Farren, N. J.; et al. Atmospheric Chemistry of 2-Amino-2-methyl-1-propanol: A Theoretical and Experimental Study of the OH-Initiated Degradation under Simulated Atmospheric Conditions. *J. Phys. Chem. A* **2021**, *125*, 7502−7519.

(9) Nielsen, C. J.; Herrmann, H.; Weller, C. Atmospheric Chemistry and Environmental Impact of the use of Amines in Carbon Capture and Storage (CCS). *Chem. Soc. Rev.* **2012**, *41*, 6684−6704.

(10) Ge, X.; Wexler, A. S.; Clegg, S. L. Atmospheric Amines − Part I. A review. *Atmos. Environ.* **2011**, *45*, 524−546.

(11) Schade, G. W.; Crutzen, P. J. Emission of Aliphatic-Amines from Animal Husbandry and their Reactions - Potential Source of N_2O and HCN. *J. Atmos. Chem.* **1995**, *22*, 319−346.

(12) Fostås, B.; Gangstad, A.; Nenseter, B.; Pedersen, S.; Sjoevoll, M.; Soerensen, A. L. Effects of NOx in the Flue Gas Degradation of MEA. *Energy Procedia* **2011**, *4*, 1566−1573.

(13) Layer, R. W. Chemistry of Imines. *Chem. Rev.* **1963**, *63*, 489−510.

(14) Gowenlock, B. G.; Thomas, K. E. The Gaseous Equilibrium of 1,3,5-Trimethylhexahydro-1,3,5-triazine and N-Methylenemethyl-amine. *J. Chem. Soc. B* **1966**, 409−410.

(15) Tuazon, E. C.; Atkinson, R.; Aschmann, S. M.; Arey, J. Kinetics and Products of the Gas-Phase Reactions of O_3 with Amines and Related-Compounds. *Res. Chem. Intermed.* **1994**, *20*, 303−320.

(16) Tuazon, E. C.; Carter, W. P. L.; Atkinson, R.; Winer, A. M.; Pitts, J. N. Atmospheric Reactions of N-Nitrosodimethylamine and Dimethylnitramine. *Environ. Sci. Technol.* **1984**, *18*, 49−54.

(17) Lazarou, Y. G.; Papagiannakopoulos, P. Kinetic Studies of the Reactions of Atomic Chlorine with N-Methylmethylenimine and 1,3,5-Trimethylhexahydro-1,3,5-triazine. *J. Phys. Chem.* **1993**, *97*, 4468−4472.

(18) Kaiser, E. W.; Wallington, T. J. Pressure Dependence of the Reaction Cl+C_3H_6. *J. Phys. Chem.* **1996**, *100*, 9788−9793.

(19) CCS Norway. https://ccsnorway.com/hse-studies/ (accessed February 8, 2022).

(20) Bunkan, A. J. C.; Tang, Y.; Sellevåg, S. R.; Nielsen, C. J. Atmospheric Gas Phase Chemistry of $CH_2=NH$ and HNC. A First-Principles Approach. *J. Phys. Chem. A* **2014**, *118*, 5279−5288.

(21) Akbar Ali, M.; Barker, J. R. Comparison of Three Isoelectronic Multiple-Well Reaction Systems: OH + CH_2O, OH + CH_2CH_2, and OH + CH_2NH. *J. Phys. Chem. A* **2015**, *119*, 7578.

(22) Antonsen, S. G.; Bunkan, A. J. C.; Mikoviny, T.; Nielsen, C. J.; Stenstrøm, Y.; Wisthaler, A.; Zardin, E. Atmospheric Chemistry of Diazomethane − an Experimental and Theoretical study. *Mol. Phys.* **2020**, *118*, No. e1718227.

(23) Hinze, J.; Curl, R. F. Infrared Spectrum of N-Methylenemethyl-amine. *J. Atm. Chem. Soc.* **1964**, *86*, 5068−5070.

(24) Stolkin, I.; Ha, T. K.; Günthard, H. H. N-Methylmethylenei-mine and Ethylideneimine: Gas- and Matrix-Infrared Spectra, Ab Initio Calculations and Thermodynamic Properties. *Chem. Phys.* **1977**, *21*, 327−347.

(25) Møller, C.; Plesset, M. S. Note on an Approximation Treatment for Many-Electron Systems. *Phys. Rev.* **1934**, *46*, 618−622.

(26) Zhao, Y.; Truhlar, D. G. The M06 Suite of Density Functionals for Main Group Thermochemistry, Thermochemical Kinetics, Noncovalent Interactions, Excited States, and Transition Elements: Two New Functionals and Systematic Testing of Four M06-class Functionals and 12 other Functionals. *Theor. Chem. Acc.* **2008**, *120*, 215−241.

(27) Dunning, T. H., Jr. Gaussian Basis Sets for use in Correlated Molecular Calculations. I. The Atoms Boron through Neon and Hydrogen. *J. Chem. Phys.* **1989**, *90*, 1007−1023.

(28) Kendall, R. A.; Dunning, T. H.; Harrison, R. J. Electron-Affinities of the 1st-Row Atoms Revisited - Systematic Basis-Sets and Wave-Functions. *J. Chem. Phys.* **1992**, *96*, 6796−6806.

(29) Knizia, G.; Adler, T. B.; Werner, H.-J. Simplified CCSD(T)-F12 Methods: Theory and Benchmarks. *J. Chem. Phys.* **2009**, *130*, 054104.

(30) Su, T. Parametrization of Kinetic Energy Dependences of Ion−Polar Molecule Collision Rate Constants by Trajectory Calculations. *J. Chem. Phys.* **1994**, *100*, 4703−4703.

(31) Curtiss, L. A.; Redfern, P. C.; Raghavachari, K. Gaussian-4 Theory. *J. Chem. Phys.* **2007**, *126*, 084108.

(32) Frisch, M. J.; Trucks, G. W.; Schlegel, H. B.; Scuseria, G. E.; Robb, M. A.; Cheeseman, J. R.; Scalmani, G.; Barone, V.; Mennucci, B.; Petersson, G. A., et al. *Gaussian 09*, Rev. C.01, Gaussian, Inc.: Wallingford CT, 2009.

(33) Frisch, M. J.; Trucks, G. W.; Schlegel, H. B.; Scuseria, G. E.; Robb, M. A.; Cheeseman, J. R.; Scalmani, G.; Barone, V.; Petersson, G. A.; Nakatsuji, H., et al. *Gaussian 16*, Rev. C.01; Gaussian Inc.: Wallingford, CT, 2016.

(34) Werner, H.-J.; Knowles, P. J.; Knizia, G.; Manby, F. R.; Schütz, M. Molpro: a General-Purpose Quantum Chemistry Program Package. *Wiley Interdiscip. Rev.: Comput. Mol. Sci.* **2012**, *2*, 242−253.

(35) Glowacki, D. R.; Liang, C.-H.; Morley, C.; Pilling, M. J.; Robertson, S. H. MESMER: An Open-Source Master Equation Solver for Multi-Energy Well Reactions. *J. Phys. Chem. A* **2012**, *116*, 9545−9560.

(36) Miller, W. H. Tunneling Corrections to Unimolecular Rate Constants, with Application to Formaldehyde. *J. Atm. Chem. Soc.* **1979**, *101*, 6810−6814.

(37) Georgievskii, Y.; Klippenstein, S. J. Long-Range Transition State Theory. *J. Chem. Phys.* **2005**, *122*, 194103.

(38) Coxon, J. A.; Foster, S. C. Radical Dependence of Spin Orbit and Λ-doubling Parameters in the X^2-Π Ground-State os Hydroxyl. *J. Mol. Spectrosc.* **1982**, *91*, 243−254.

(39) Poling, B. E.; Prausnitz, J. M.; O'Connel, J. P. *The Properties of Gases and Liquids*; McGraw-Hill: 2001.

(40) Lee, T. J.; Taylor, P. R. A Diagnostic for Determining the Quality of Single-Reference Electron Correlation Methods. *Int. J. Quant. Chem. Symp.* **1989**, *36*, 199−207.

(41) Janssen, C. L.; Nielsen, I. M. B. New Diagnostics for Coupled-Cluster and Møller−Plesset Perturbation Theory. *Chem. Phys. Lett.* **1998**, *290*, 423−430.

(42) Lee, T. J. Comparison of the T_1 and D_1 Diagnostics for Electronic Structure Theory: a New Definition for the Open-Shell D_1 Diagnostic. *Chem. Phys. Lett.* **2003**, *372*, 362−367.

(43) Hirota, E.; Morino, Y. Microwave Spectrum of Propylene. I. Molecular Structure (r_s) and Orientation of Dipole Moment. *J. Chem. Phys.* **1966**, *45*, 2326−2327.

(44) Durig, J. R.; Guirgis, G. A.; Bell, S. Torsional Spectrum and Ab-initio Calculations for Propene. *J. Phys. Chem.* **1989**, *93*, 3487−3491.

(45) Wlodarczak, G.; Demaison, J.; Heineking, N.; Csaszar, A. G. The Rotational Spectrum of Propene - Internal Rotation Analysis and Ab-Initio and Experimental Centrifugal Distortion Constants. *J. Mol. Spectrosc.* **1994**, *167*, 239−247.

(46) *NIST Computational Chemistry Comparison and Benchmark Database*; (accessed February 8).

(47) IUPAC Task Group on Atmospheric Chemical Kinetic Data Evaluation *Data Sheet II.A2.7 HOx_VOCS*; http://iupac.pole-ether.fr (accessed February 8, 2022).

(48) Finlayson-Pitts, B.; Pitts, J. N. *Chemistry of the Upper and Lower Atmosphere: Theory, Experiments, and Applications*; Academic Press: San Diego, CA, 2000.

(49) Wayne, R. P.; Barnes, I.; Biggs, P.; Burrows, J. P.; Canosamas, C. E.; Hjorth, J.; Lebras, G.; Moortgat, G. K.; Perner, D.; Poulet, G.; et al. The Nitrate Radical - Physics, Chemistry, and the Atmosphere. *Atmos. Environ., Part A* **1991**, *25*, 1−203.

(50) Lazarou, Y. G.; Kambanis, K. G.; Papagiannakopoulos, P. Gas-Phase Reactions of $(CH_3)_2N$ Radicals with NO and NO_2. *J. Phys. Chem.* **1994**, *98*, 2110−2115.

(51) Manion, J. A.; Huie, R. E.; Levin, R. D.; Burgess, D. R., Jr.; Orkin, V. L.; Tsang, W.; McGivern, W. S.; Hudgens, J. W.; Knyazev, V. D.; Atkinson, D. B., et al. *NIST Chemical Kinetics Database, NIST Standard Reference Database 17*, Version 7.0 (Web Version), Release 1.6.8, Data version 2015.09 https://kinetics.nist.gov/kinetics/ (accessed February 08, 2022).

(52) Zhao, Y.; Tishchenko, O.; Gour, J. R.; Li, W.; Lutz, J. J.; Piecuch, P.; Truhlar, D. G. Thermochemical Kinetics for Multireference Systems: Addition Reactions of Ozone. *J. Phys. Chem. A* **2009**, *113*, 5786−5799.

(53) Wheeler, S. E.; Ess, D. H.; Houk, K. N. Thinking Out of the Black Box: Accurate Barrier Heights of 1,3-Dipolar Cycloadditions of Ozone with Acetylene and Ethylene. *J. Phys. Chem. A* **2008**, *112*, 1798−1807.

(54) Atkinson, R.; Baulch, D. L.; Cox, R. A.; Crowley, J. N.; Hampson, R. F.; Hynes, R. G.; Jenkin, M. E.; Rossi, M. J.; Troe, J. Evaluated Kinetic and Photochemical Data for Atmospheric Chemistry: Volume I - Gas Phase Reactions of O(x), HO(x), NO(x) and SO(x) Species. *Atmospheric Chemistry and Physics* **2004**, *4*, 1461−1738.

(55) Stratmann, R. E.; Scuseria, G. E.; Frisch, M. J. An Efficient Implementation of Time-Dependent Density-Functional Theory for the Calculation of Excitation Energies of Large Molecules. *J. Chem. Phys.* **1998**, *109*, 8218−8224.

(56) Teslja, A.; Nizamov, B.; Dagdigian, P. J. The Electronic Spectrum of Methyleneimine. *J. Phys. Chem. A* **2004**, *108*, 4433−4439.

(57) Bonačić-Koutecký, V.; Michl, J. Photochemical syn-anti Isomerization of a Schiff Base: A Two-Dimensional Description of a Conical Intersection in Formaldimine. *Theor. Chim. Acta* **1985**, *68*, 45−55.

(58) Piel, F.; Müller, M.; Winkler, K.; Skytte af Sätra, J.; Wisthaler, A. Introducing the Extended Volatility Range Proton-Transfer-Reaction Mass Spectrometer (EVR PTR-MS). *Atmos. Meas. Technol.* **2021**, *14*, 1355−1363.

(59) Papanastasiou, D. K.; Bernard, F.; Burkholder, J. B. Atmospheric Fate of Methyl Isocyanate, CH_3NCO: OH and Cl Reaction Kinetics and Identification of Formyl Isocyanate, HC(O)-NCO. *ACS Earth and Space Chemistry* **2020**, *4*, 1626−1637.

(60) Müller, M.; Eichler, P.; D'Anna, B.; Tan, W.; Wisthaler, A. Direct Sampling and Analysis of Atmospheric Particulate Organic Matter by Proton-Transfer-Reaction Mass Spectrometry. *Anal. Chem.* **2017**, *89*, 10889−10897.

(61) Prinn, R. G.; Weiss, R. F.; Miller, B. R.; Huang, J.; Alyea, F. N.; Cunnold, D. M.; Fraser, P. J.; Hartley, D. E.; Simmonds, P. G. Atmospheric Trends and Lifetime of CH_3CCl_3 and Global OH Concentrations. *Science* **1995**, *269*, 187−192.

(62) Atkinson, R. Kinetics and Mechanisms of the Gas-Phase Reactions of the NO_3 Radical with Organic Compounds. *J. Phys. Chem. Ref. Data* **1991**, *20*, 459−507.

(63) Wang, L.; Lal, V.; Khalizov, A. F.; Zhang, R. Heterogeneous Chemistry of Alkylamines with Sulfuric Acid: Implications for Atmospheric Formation of Alkylaminium Sulfates. *Environ. Sci. Technol.* **2010**, *44*, 2461−2465.

(64) Heicklen, J. The Removal of Atmospheric Gases by Particulate Matter. *Atmospheric Environment (1967)* **1981**, *15*, 781−785.

▣ Recommended by ACS

Influence of $H_2SO_4 \cdots H_2O$ and $(H_2SO_4)_2$ on the Hydrolysis of Formaldehyde: A Potential Source of Methanediol in the Troposphere

Yongqi Zhang, Ke Zhou, *et al.*

NOVEMBER 22, 2022
ACS EARTH AND SPACE CHEMISTRY   READ ◱

Unusual In-plane Aromaticity Facilitates Intramolecular Hydrogen Transfer in Long-Bonded *cis*-Isonitrosyl Methoxide

Punhasa S. Senanayake, Marat R. Talipov, *et al.*

SEPTEMBER 01, 2022
THE JOURNAL OF PHYSICAL CHEMISTRY A   READ ◱

Temperature and Pressure-Dependent Rate Constants for the Reaction of the Propargyl Radical with Molecular Oxygen

Tien V. Pham, Hue Minh Thi Nguyen, *et al.*

SEPTEMBER 07, 2022
ACS OMEGA   READ ◱

Charge Transfer Reactions between Water Isotopologues and Kr^+ ions

Andriana Tsikritea, Brianna R. Heazlewood, *et al.*

JANUARY 31, 2022
ACS PHYSICAL CHEMISTRY AU   READ ◱

Get More Suggestions >